



FACULDADE DE
CIÊNCIAS E TECNOLOGIA
UNIVERSIDADE NOVA DE LISBOA

Hydrogen Permeation in Parabolic Trough Receivers

Helena Mafalda de Sousa Reis Orvalho

MASTERTHESIS

submitted in Faculdade de Ciências e Tecnologia da Universidade Nova de Lisboa,
in partial fulfillment of the requirements for the degree of

Master

in

Materials Engineering

Monte da Caparica,

July 2009

Supervised by:

Dr Marc Moellenhof

Prof. Isabel Ferreira

Acknowledgements

First I would like to thank Professor Isabel Ferreira for taking time out from her busy schedule, agree to be my Supervisor and opening the door to such fantastic opportunity.

I'm also indebted to my external supervisor Dr Marc Moellenhoff for making himself always available, giving great advice and encouragement even though he was often buried with work.

I also want to express my gratitude to Tim Gnaedig, Zdenek Hacker, Dr Jan Schulte-Fischedick and Matthias Mueller whose expertise, understanding, and patience helped me to go through all the difficulties faced. I wish also to thank Christina Albers for taking the trouble of reading thoroughly the thesis and making suggestions.

I'm also grateful to all the workshop staff especially Matthias Mueller, Rino, Adolf, Karl-Heinz, Gerald and Sebastian for all the assistance provided in the building process.

I must also thank my colleagues and friends : Jens, Sullivan, Michael, Klaus, Sofia, Kamel, Sebastian, Marc, Zdenec, Stefan, Alex, Celia and Matthias not only for a great work environment but also for making me feel i was at home.

I won't ever be able to convey my appreciation fully to Matthias and Marion Mueller for taken me under their wing during the time i've been in Mitterteich: I owe them my eternal gratitude for everything they did.

Finally a very special thanks to my family for their unconditional love and support not only during the time of this thesis but throughout my life, without which I wouldn't be able to have gone this far.

Abstract

The continued economic and population development puts additional pressure on the already scarce energetic sources. Thus there is a growing urge to adopt a sustainable plan able to meet the present and future energetic demands.

Since the last two decades, solar trough technology has been demonstrating to be a reliable alternative to fossil fuels. Currently, the trough industry seeks, by optimizing energy conversion, to drive the cost of electricity down and therefore to place itself as main player in the next energetic age.

One of the issues that lately have gained considerable relevance came from the observation of significant heat losses in a large number of receiver modules. These heat losses were attributed to slow permeation of traces of hydrogen gas through the steel tube wall into the vacuum annulus. The presence of hydrogen gas in the absorber tube results from the decomposition of heat transfer fluid due to the long-term exposure to 400°C.

The permeated hydrogen acts as heat conduction mean leading to a decrease in the receivers performance and thus its lifetime. In order to prevent hydrogen accumulation, it has been common practice to incorporate hydrogen getters in the vacuum annulus of the receivers. Nevertheless these materials are not only expensive but their gas absorbing capacity can be insufficient to assure the required level of vacuum for the receivers to function.

In this work the building of a permeation measurement device, vulnerabilities detected in the construction process and its overcome are described. Furthermore an experimental procedure was optimized and the obtained permeability results, of different samples were evaluated. The data was compared to measurements performed by an external entity. The reliability of the comparative data was also addressed.

In the end conclusions on the permeability results for the different samples characteristics, feasibility of the measurement device are drawn and recommendations on future line of work were made.

Notation

List of frequently used symbols

a	activity	H	activation energy
c	concentration	H_D, H_S, H_ϕ	activation energy of D , S and ϕ
c_1	concentration at the feed side	K	compression ratio
c_2	concentration at the permeate side	J	flux
d_i	inner diameter	L	length
d_o	outer diameter	M	metal
k	Boltzmann constant	P	pressure
l	thickness	P_0	pre-exponential factor of P
m	mass in g	Q	gas flow (general term)
n	number of particles in mol	Q_0	outgassing flow
r	pressure exponent	Q_T	throughput
s	pumping speed	Q_ϕ	permeation gas flow
t	time	R	universal gas constant
u	drift velocity	S	solubility
x	coordinate	S_0	pre-exponential factor of S
y	ordinate	T	temperature
A	area	U	potential
A_{i_s}	inner superficial area	V	volume
Ar	molar mass in g/mol	W	fit parameter
B	mobility	Z	fit parameter
C	fit parameter	ϕ	permeability
D	diffusivity	ϕ_0	pre-exponential factor of ϕ
D_0	pre-exponential factor of D	μ	chemical potential
F	force	μ^0	standard chemical potential at standard conditions, $T = 298,15$ K; $P = 101325$ Pa
G	capacity if the getter		






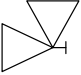
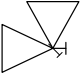

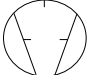

Subscripts

<i>Bo</i>	grain boundary
<i>G</i>	grain
<i>Gter</i>	getter

List of Abbreviations and Acronyms

bcc	body centered cubic
fcc	face centered cubic
hcp	hexagonal closed packed
ASS	austenitic stainless steel
CMR	capacitance diaphragm gauge
DPO	diphenyl oxide
HCE	heat conductive element
HS	heating system
HTF	heat transfer fluid
HV	high vacuum
IPP	Institute fuer Plasma Physik
LD	literature data
PID	proportional integral derivative controller
PKR	full range gauge
PMD	permeation measurement device
PS	pumping stage
PTPP	parabolic trough power plant
QMS	quadrupol mass spectrometer
RVP	rotary vane pump
TP	turbo molecular pump
UHV	ultra high vacuum
VA	vacum annulus
VV	valve

Vacuum Symbols

	KF connection
	CF connection
	flexible connection
	feedtrough
	pressure gauge
	corner valve
	needle valve
	manual valve
	rotary vane pump
	turbomolecular pump

Contents

Acknowledgements	i
Abstract	ii
Notation	iii
1 Introduction	1
1.1 Concentrated Solar Thermal Technology	1
1.2 Parabolic Trough Technology	3
1.3 Brief Presentation of the Company and Product	4
1.3.1 Schott Solar Trough Receivers	4
1.4 Hydrogen Problematic	5
1.4.1 Thermal Decomposition of the Heat Transfer Fluid	5
1.5 Aim of the Present Work	7
2 Theoretical Background	8
2.1 Fundamental Equations	8
2.2 Crystalline and Defect Structures in Metals	9
2.3 Mechanism of Hydrogen Migration in Metals	10
2.4 Diffusion	10
2.4.1 Phenomenological Description	10
2.4.2 Atomistic Description	12
2.5 Permeation	13
2.5.1 Phenomenological Description	13
2.5.2 Experimental Determination of the Permeability	15
2.6 Factors that Influence the Permeability	15
2.6.1 Cold Working, Heat Treatments and Alloying Elements	15
2.6.2 Surface Condition	15
3 Materials and Methods	18
3.1 Initial and Final Permeation Measurement Device Description	18
3.1.1 Vacuum Components	21
3.1.2 Heating System	23
3.1.3 Temperature Regulation, Control and Data Recorders	24
3.1.4 Measuring Components	27
3.2 Problems Faced and Respective Resolution	30
3.2.1 Heating System	30
3.2.2 Temperature Regulation, Control and Data Recording	32
3.2.3 Sample	32
3.2.4 Vacuum Components	33

3.2.5	Measuring Components	34
3.3	Specimens	35
3.3.1	Sample Description	35
3.3.2	Probe Assembly	35
3.4	Experimental Procedure	36
3.4.1	Procedure Description	36
3.5	Temperature Calibration	39
4	Analysis of the Results	42
4.1	Results from Institute fuer Plasma Physik	42
4.1.1	Experimental Details	42
4.1.2	Data Analysis	43
4.2	Analysis of the Experimental Data	43
4.2.1	Area of the Sample and Pumping Speed	43
4.2.2	Determination of the Steady State Flux and Permeability	43
4.2.3	Error Estimation	45
5	Discussion	46
5.1	Reliability of data from IPP	46
5.2	Experimental Data	47
5.3	Comparison of Data	48
6	Conclusions and Recommendations on Future Line of Work	49
	Bibliography	52

List of Figures

1.1	Concentrated Solar Thermal Technologies	2
1.2	Concentration type and working temperature of solar thermal technologies	3
1.3	Schotts PTR 70 Receiver	4
1.4	Components of the Heat Transfer Fluid	5
1.5	Cleavage reactions of biphenyl	6
1.6	Cleavage reactions of DPO	6
2.1	Definition of the flux	8
2.2	FCC structure	9
2.3	One dimensional description of Fick's laws	12
2.4	Mechanisms of diffusion	13
2.5	Schematic of the mechanism of permeation for two atomic gases	14
3.1	Measuring chambers in the final permeation device	19
3.2	Final Permeation Measurement Device Scheme	20
3.3	Turbo pump section	21
3.4	Rotary Vane Pump schematic representation	22
3.5	Isolation between the heating system and heating wire	23
3.6	Initial and final heating system	24
3.7	PID loop tuning temperature curves	25
3.8	Samples surface temperature curve for the initial heating system	26
3.9	Samples surface temperature curve for the late heating system	26
3.10	Functioning Principle of QMS 200	27
3.11	QMS measurement profile	28
3.12	Diaphragm capacitive gauges working principle	29
3.13	Pirani Circuit	29
3.14	Penning Gauge	30
3.15	Cause effect diagram of the main problems faced	31
3.16	Behaviour of the heating parts in consecutive trials	33
3.17	Influence of the TP breakdown in the measurement results	34
3.18	Contamination of the cathode of the full range gauge	35
3.19	Assembled probe	36
3.20	Detailed view of a measuring chamber, full range gauge positioning, intermediary pipping and flow direction	37
3.21	Measurement profile and stage identification	37
3.22	Temperature Profile of the sample in chamber 1	40
3.23	Temperature Profile of the sample in chamber 2	40
4.1	IPP Permeation Measurement Device	42
4.2	Producer A flux versus time curves	44
4.3	Producer D flux versus time curves, average curve fitting and respective parameters	44

5.1	Permeability versus Temperature plot for IPP and literature data	47
5.2	Surface condition after a measurement	47

List of Tables

1.1	Status of Concentrated Solar Power Overview in 2007	3
3.1	Turbomolecular pump characteristics	22
3.2	Rotary Vane Pump models, pumping speed for nitrogen and ultimate pressure . .	23
3.3	Effects on increasing Parameters	24
3.4	Temperatures along the Sample and average for each chamber	41
4.1	Flux and permeability for the experimental results	45
4.2	Relative Errors	45
6.1	Differences between initial and current permeation measurement devices	50

Chapter 1

Introduction

An overwhelming consensus of scientific opinion agrees human activities, such as burning fossil fuels, are responsible for the relentless build-up of greenhouse gases in the earth's atmosphere and consequent global climate change. This process is already disrupting ecosystems and through the increasing risk of hunger, diseases, flooding and water shortages is estimated to be causing around 150,000 additional deaths per year and threatening millions of people [1].

On the other hand, fossil fuels - oil gas and coal - are becoming scarcer and more expensive to produce. This adding to the over-reliance on energy imports from a few, often politically unstable countries contribute to the increasing social and economical instability.

If this present perspectives seem already dark, the future is not also much brighter. The development of global energy demand is driven by two key factors:

- Population development: according to the United Nations population development projections, the world's population is expected to grow from 6,3 to almost 8,9 billion [1] by 0,78% over the period 2003 to 2050.
- Industrial development and economic growth

This scenario reveals the unfeasibility of our actual energetic plan and drives us to the evident conclusion that, sooner or later, it will have to change.

Renewable energies provide a real and mature solution to our future that combined with the smart use of energy can deliver half of the worlds needs by 2050. [1]

1.1 Concentrated Solar Thermal Technology

Over 99.9% of the available flow of renewable energy on Earth is constituted by resources such as wind and wave power, hydroelectricity, biomass and solar radiation.

Solar radiation consists of direct and diffuse irradiation. If the skies are overcast, only diffuse radiance is available.

Direct solar radiation reaches the earth surface with a density (kW/m^2) adequate for heating systems but not for an efficient thermodynamic cycle to produce electricity. The density has thus to be increased, through the use of mirrors or lenses that concentrate the incoming solar radiation in a point or along a line. The most common types of concentrating solar thermal systems are shown in figures 1.1 and 1.2. We have:



Figure 1.1: Concentrated Solar Thermal Technologies; top: Power Tower power plant PS10 in Sanlucar, Spain [2] (left) and Dish Stirling modules in Solar Two, California, USA [3] (right); bottom: Fresnel [4] (left) and Parabolic Troughs [4] (right) in Plataforma Solar de Almeria, Spain

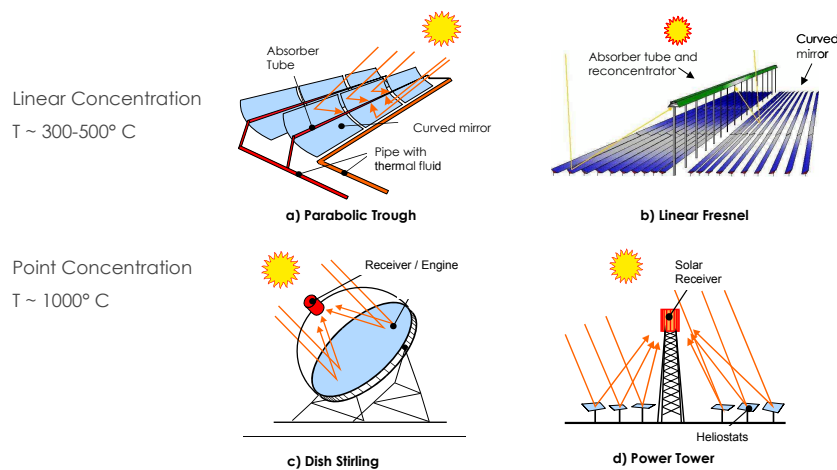
1. Power tower systems that consist of fields where thousands of sun-tracking mirrors (heliostats) direct insolation to a receiver. The receiver is placed on top of a tall tower where a molten salt heat-transfer fluid is heated and driven to the ground based steam generator. The steam drives then turbines that activate the generator and electricity is produced.
2. Dish Stirling systems that generate power by using parabolically arranged mirrors to reflect sunlight onto a small focal receiver, the stirling engine, thereby heating a gas chamber connected to a piston and drive shaft. The drive shaft powers a generator and produces electricity.
3. Fresnel technology uses horizontal flat mirror facets that track the sun. The energy is also transferred to a heat exchanger using a heat transfer medium
4. Parabolic troughs where rows of trough-shaped mirrors direct insolation to a receiver tube placed along its focal axis. The focused radiation heats the heat-transfer fluid (HTF) which goes through a heat exchanger that generates steam and powers the conventional turbines.

Table 1.1 gives an overview of the maturity status of each concentrated solar power system.

Power supply during unfavourable weather and at night is possible due to thermal energy storage systems. Millions of liters of HTF circulating in the solar field can function as thermal storage medium offering a considerable capacity.

Table 1.1: Status of Concentrated Solar Power Overview in 2007 [5]

Technology	Status	Projects ahead	Location
Parabolic Trough	Commercial	50-150 MW	Spain, India, Mexico, Egypt, Morocco, Crete, Jordan, USA, South Africa
Linear Fresnel	Prototype, demonstration	1-5 MW pilot plant	California
Solar Power Tower	Prototype, demonstration	PS10 (10 MW steam cycle)	Spain
Parabolic Dish	Prototype, demonstration	EURO-DISH, 10 kW series, Solar One and Two, 500 and 850 MW Power Plant	California, USA

**Figure 1.2:** Concentration type and working temperature of solar thermal technologies [6]; Linear concentration technologies operate in temperatures ranging 300-500°C while point concentration technologies in temperatures around 1000°C

There is also a possibility of combining solar thermal power plants with fossil energy sources. Since solar fields feed their heat energy into a conventional steam turbine, they can be easily integrated in latest generation and relatively clean, natural gas fired combined cycle power plants.

1.2 Parabolic Trough Technology

Parabolic trough technology has the highest efficiency at lowest energy production costs and material requirements of all solar thermal power plant technologies.

Since the materials used, such as steel, glass and concrete, are available and affordable worldwide, parabolic trough power plants (PTPP) can be constructed and operated by local labour. It

is also a proven technology that has already achieved market maturity and shown its reliability: the first PTPP was built in Mojave's Desert in 1984. By 1991, nine solar fields with 2,5 million square meters of concentrating reflector surface were erected on more than 7 km². So far they have been running with a total output of 354 MW and fed more than 12 billion kW hours into the California grid, earning nearly 1,6 billion US dollars. Its technical availability has always been over 98 percent and the 25 years planned lifetime of the parabolic trough field is expected to be exceeded by far [7].

1.3 Brief Presentation of the Company and Product

Schott is a 125 year old multinational, technology-based group that develops and manufactures specialty materials, components and systems for diverse markets: household appliances, pharmaceutical industries, electronics, optics, automotive and solar energy.



Figure 1.3: Schotts PTR 70 Receiver [8]; it consists of an absorber tube enclosed in vacuum by a glass tube with metallic bellows and seal

The business unit Schott Solar AG is one of the leading solar industry companies worldwide. It offers a wide range of future-oriented products and solutions for almost all photovoltaic and solar thermal applications.

In the segment of concentrated solar power, SCHOTT Solar CSP GmbH offers high-output receivers (figure 1.3) that are a key component in solar thermal parabolic trough power plants.

1.3.1 Schott Solar Trough Receivers

The receivers, also known as heat conductive elements (HCE), consist of an absorber tube enclosed in vacuum by a glass tube.

The absorber tube is 4 meter long austenitic stainless steel (ASS) tube with a multilayer solar-selective absorber surface.

The cermet absorber coating is produced in a reactive sputtering and its optical properties allow to achieve high solar absorbance and low emittance at the HCE working temperatures, maximizing solar gains and minimizing heat losses.

The glass tube is coated with anti-reflective films for high solar transmittance on both surfaces to minimize the reflective losses and maximize the solar transmittance.

The vacuum pressure in the vacuum annulus (VA) is kept below 0,1 Pa to suppress heat conduction losses. To maintain such vacuum levels, getters designed to absorb gas molecules, are installed in the vacuum space. The receivers also include an evaporable barium getter used to monitor the vacuum in the receiver. The barium getter presents a silver appearance that turns white if the vacuum level is compromised.

The junction between the absorber tube and glass envelope is kept stable by the use of bellows made of metal and a glass to metal seal made from a material combination with adjusted coefficients of thermal expansion

1.4 Hydrogen Problematic

Observations in several solar fields [9] have revealed significant heat losses in a large number of receiver modules. These heat losses have been attributed to the slow permeation of gas traces through the steel tube wall into the VA, compromising its thermal insulation capacity and thereby shortening the receivers lifetime. In order to absorb these traces of hydrogen gas formed over time it has been common practice to incorporate hydrogen getters in the VA. However these materials are expensive and the long-term exposure of the organic thermal oil to 400°C can lead to hydrogen pressures that exceed the getters gas-absorbing capacity.

1.4.1 Thermal Decomposition of the Heat Transfer Fluid

The HTF that flows inside of the HCE, is known under the trademark of Therminol VP-1 or Dowtherm A. Its composition is 73,5% diphenyl oxide (DPO) and 26,5% biphenyl in the eutectic formulation [10]. In spite of having a boiling point of 257°C, the HTF has been successfully

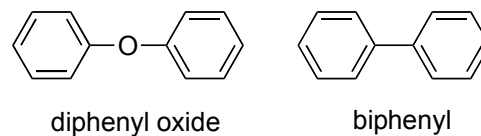


Figure 1.4: Components of the Heat Transfer Fluid [10]; diphenyl oxide and biphenyl

used above this temperature in PTPP for many years without a significant decrease in the performance. This might be due to its low thermal degradation rates as it was study in reference [11]. In this work, Dowtherm A was heated at 425°C for 120 h which resulted in the formation of a mixture composed by: a) gaseous products consisting of hydrogen gas, 44% of the total gas volume, and small hydrocarbons, and b) a fraction containing the aromatic compounds.

Thermal Decomposition of Biphenyl and DPO

The direct thermal cleavage of biphenyl and diphenyl oxide (figure 1.6) forms phenyl radicals, and phenoxy [12, 13]. The resultant highly reactive hydrogen atoms may either recombine or attack the biphenyl and DPO. These steps altogether can then initiate a chain reaction leading to the production of benzene, polyphenyl compounds (e.g. terphenyl), and also more hydrogen atoms that ultimately recombine to form hydrogen gas [14] as it is shown in figures 1.5 and 1.6.

Hydrogen Pressures in Parabolic Trough Receivers

There is still no consensus in the several values reported in field tests. In this work we are going to consider a maximum partial pressure of 20 mbar.

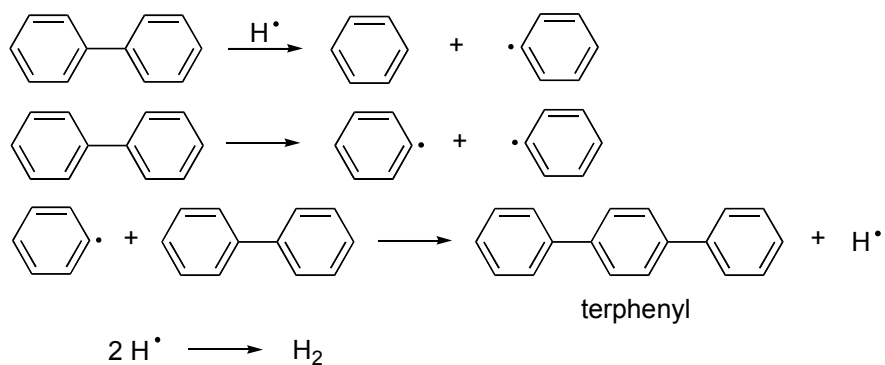


Figure 1.5: Cleavage reactions of biphenyl [10]; either by highly reactive hydrogen atoms (first reaction), thermal cleavage (second reaction) and consequent formation of poliphenyls and molecular hydrogen

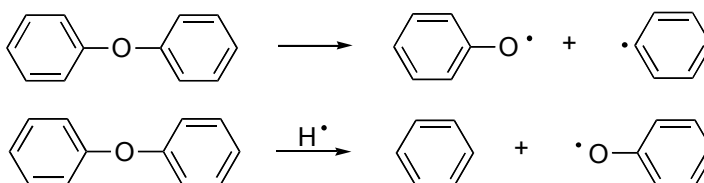


Figure 1.6: Cleavage reactions of DPO [10]; either by thermal cleavage (first reaction) and hydrogen attack (second reaction)

1.5 Aim of the Present Work

The aims of the present work were:

- to put up a permeation measurement equipment,
- the assessment of its reliability through the evaluation of the measurement results,

The ability of measuring the permeability constitutes the first step towards the development of permeation resistant barriers. An effective permeation barrier will then allow the reduction of heat losses and necessary getter amount required to keep the receivers running for 25 years.

This thesis is the follow up of works which came up with a prototype of a permeation measurement device (PMD).

The prototype was rebuilt in this work and subjected to a longer period of testing that helped to identify and resolve its main limitations. Chapter 3 presents the methods previously established, the ones currently used and the encountered problems and respective solutions. It also gives some details on specimen preparation, measurement procedure and temperature regulation and calibration stages

The assessment of the PMD reliability is made through the contrast between the obtained measurement results with the ones obtained by an external entity performed on different samples from several producers.

In Chapter 4 is explained (1) how the permeability and activation energy were determined from the provided flux values for the comparative data and (2) how the permeability and respective error were obtained from pressure values of the experimental data. In the first section of chapter 5 the comparison data is evaluated using several literature references. Some considerations on the results obtained for the oxidized and unoxidized samples are also made. In the second section the experimental results are analyzed and put side by side with the comparison data. The discussion of the different conditions is made.

The following chapter gives an overview of the theoretical background that enfolds the permeation subject not only in the mechanistic plan but also in the experimental point of view.

Chapter 2

Theoretical Background

2.1 Fundamental Equations

The behaviour of gas molecules in high vacuum (HV, according to Pfeiffer Vacuum, pressures between 10^{-1} , 10^{-5} Pa), and ultra high vacuum (UHV, pressures under 10^{-5} Pa) can be described by the ideal gas law:

$$n = \frac{PV}{RT} \quad (2.1)$$

Where n is represented in the SI system by mol, P is the gas pressure in Pa, V the gas volume (m^3), R the ideal gas constant ($\text{J mol}^{-1}\text{K}^{-1}$) and T the gas temperature (K).

RT is often considered to be constant throughout the whole system for the whole period of interest. Therefore is often placed on the left side of equation describing in this way the pumping of gas (the throughput of gas) as:

$$\frac{dn}{R}T = Q \quad (2.2)$$

which units are $\text{Pa m}^3\text{s}^{-1}$.

In terms of pressure and volume,

$$Q = \frac{d(PV)}{dt} \quad (2.3)$$

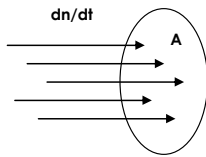


Figure 2.1: Definition of the flux, J [15]; the amount of particles dn crosses the area A in a period of time dt

The transport of gases in permeation processes can also be described by the flux, J . The flux is defined as the rate of particles per unit of area (see figure 2.1),

$$J = \frac{1}{A} \frac{dn}{dt} \quad (2.4)$$

its units come in $\text{mol m}^{-2}\text{s}^{-1}$.

Substituting 2.1 in 2.3 and the result in 2.4, we obtain the relationship between flux and gas flow:

$$J = \frac{1}{ART} Q \quad (2.5)$$

If in equation 2.3, P is constant, the throughput can be expressed by a simple equation:

$$Q = sP, \quad (2.6)$$

where s is the pumping speed, defined as the volumetric flow through the pump's intake port, and presented usually in l/s.

$$s = \frac{dV}{dt} \quad (2.7)$$

The nominal pumping speed is independent of the pressure in the molecular flow state [16] and therefore in the predominating vacuum regime ($< 10^{-4}$ mbar or 10^{-2} Pa).

The effective pumping speed will correspond only to the inlet speed of a particular pump (or the pump system) if the pump is joined directly to the vessel or system.

2.2 Crystalline and Defect Structures in Metals

The mechanism and rate of permeation are strongly related to the structure of the bulk material. Metals and alloys are characterized by their compact crystal structure thus three types of crystal structure are predominant: face-centred cubic (fcc), body centred cubic (bcc) and hexagonal closed packed (hcp). Austenitic stainless steels (ASS) have a fcc structure, high content of alloying elements and a complex chemical composition.

In the fcc structure each of the corner atoms is the corner of another cube and shared among

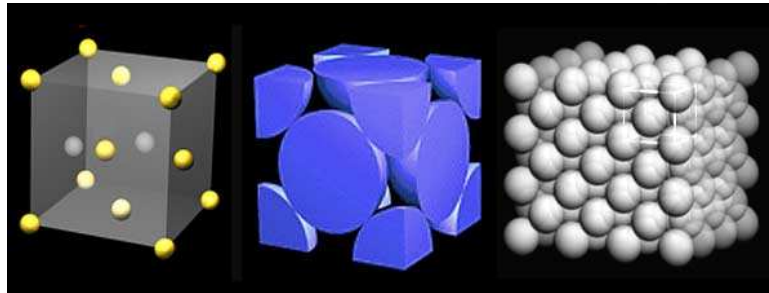


Figure 2.2: FCC structure [17]

eight unit cells. Each of its six face centered atoms is shared with an adjacent atom. Since 12 of its atoms are shared, it is said to have a coordination number of 12. The fcc unit cell consists then of a net total of four atoms: eight eighths from corner atoms and six halves of the face atoms as shown in the middle image of figure 2.2. In the fcc lattice the octahedral positions have the largest free volume [18].

The structure of metals contains defects of various dimensionalities [18]:

- zero-dimensional defects or point defects such as impurity atoms in a pure metal, vacancies and self interstitials where the concentration of the latest increases with increasing temperature,
- one-dimensional or linear defects, such as dislocations that may be produced in metals by plastic deformation,
- two-dimensional structural defects which include stacking faults, inter phase boundaries and internal surfaces of micro voids, micro cracks and grain boundaries.

2.3 Mechanism of Hydrogen Migration in Metals

When molecules of the gas phase hit the surface of a solid, stick on it with a certain probability in an event called adsorption. Desorption is the opposite process of adsorption. Absorption denotes migration into the bulk of the solvent.

In the absorption process of two atomic gases like hydrogen, molecules first adsorb physically on the surface, dissociate and become chemically adsorbed as it is expressed in equation 2.8.



The adsorbed gas atoms then exchange their surface place with the first interstitial layers within the solid (absorption). These details vary from metal to metal, and also from one type of crystallographic surface plane to another.

The general term given to adsorption, desorption and absorption is sorption. The sorption of gases in metals can be described by the equation 2.9:

$$c = SP^r \quad (2.9)$$

If the gas does not dissociates, $r = 1$ and the equation is called Henry's law. If the gas dissociates, $r = 1/2$ and the equation is called Sievert's law:

$$c = SP^{1/2} \quad (2.10)$$

where c is the concentration in mol m^{-2} and S the solubility in $\text{mol m}^{-3} \text{ Pa}^{-1/2}$ which follows the Arrhenius type dependency:

$$S = S_0 \exp\left(\frac{-H_S}{RT}\right) \quad (2.11)$$

All data for hydrogen solubility in pure metals and solid solutions has been found to obey Sievert's Law [19].

2.4 Diffusion

Solid state diffusion can be defined as the movement and transport of atoms in solid phases due to the presence of imperfections or defects. It is responsible for numerous chemical reactions or micro structural changes in solids and plays a role of high importance in the permeation.

The diffusion processes described in the next section are considered to take place in an isothermal, isobaric and field-free system.

2.4.1 Phenomenological Description

Let us consider the homogeneous transport of particles across a plane under a driving force F . The particle flux through 1 m^2 of the plane is given by the product of the volume concentration c of the particles at the plane and its average migration or drift velocity u :

$$J \left(\frac{\text{particles}}{\text{m}^2\text{s}} \right) = c \left(\frac{\text{particles}}{\text{m}^3} \right) \times u \text{ (m/s)} \quad (2.12)$$

for uncorrelated movements the drift velocity is proportional to the driving force F exerted on the particle:

$$u = BF \quad (2.13)$$

where B is termed the mobility ("*Beweglichkeit*") and is defined as the average drift velocity per unit of driving force.

The driving force is given by the negative value of the potential gradient normal to the cross-sectional area:

$$F = -\frac{dU}{dx} \quad (2.14)$$

where U is the potential. The negative signal results from the fact that transport takes place from higher to lower values of U .

The result of the combination of equations 2.13 and 2.14 is

$$J = -cB\frac{dU}{dx} \quad (2.15)$$

if the particles or atoms move in a chemical potential gradient, the potential equals the chemical potential: $U = \mu$ and then we have:

$$J = -cB\frac{d\mu}{dx} \quad (2.16)$$

μ is related to the activity a through

$$\mu = \mu^0 + kT \ln a \quad (2.17)$$

where k is the Boltzmann constant and μ^0 is the standard chemical potential.

If ideal conditions are assumed, the activity can be set equal to the mole fraction or concentration of particles. The chemical potential gradient is then given by:

$$\frac{d\mu}{dx} = kT \frac{d \ln c}{dx} = \frac{kT}{c} \frac{dc}{dx} \quad (2.18)$$

Substituting the expression 2.18 in 2.17, the particle flux becomes:

$$J = -cB\frac{d\mu}{dx} = -BkT\frac{dc}{dx} \quad (2.19)$$

$-BkT$ is termed either diffusion coefficient or diffusivity. It is expressed by D and its units are m^2s^{-1} .

The diffusivity is dependent of concentration and temperature dependent, and expresses the ability of atoms or molecules to move in a solvent material under the influence of a concentration gradient. It also can be described by the Arrhenius-type equation 2.20:

$$D = D_0 \exp\left(\frac{-H_D}{RT}\right) \quad (2.20)$$

Equation 2.19 then takes the form of 2.21 and entitled Fick's first law:

$$J = -D\frac{dc}{dx} \quad (2.21)$$

The use of Ficks first law requires a fixed concentration gradient. However the diffusion movement of the dissolved atoms leads in general to a change of the concentration. It is then more convenient to measure the variation of concentration with time.

Considering the mass conservation principle, the transient state is described by the second law of Fick which has the form:

$$\frac{\partial c}{\partial t} = \frac{\partial}{\partial x}\left(D\frac{\partial c}{\partial x}\right) \quad (2.22)$$

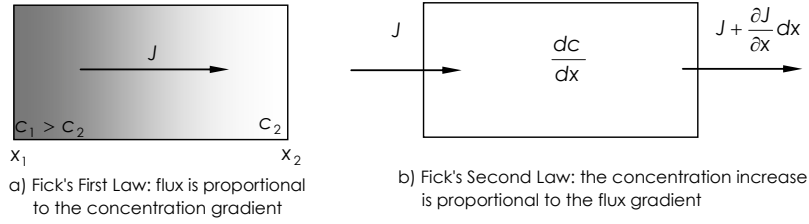


Figure 2.3: One dimensional description of Fick's laws [15]

if the diffusion coefficient is constant, the expression for Fick's second law becomes:

$$\frac{\partial c}{\partial t} = D \frac{\partial^2 c}{\partial x^2} \quad (2.23)$$

Both Fick's laws are schematically illustrated in figure 2.3

Considering an element with area A and thickness l , where $l \ll \sqrt{A}$. The concentration at the feed side, $x = 0$, and permeate side, $x = l$, may be termed c_1 and c_2 , respectively.

Initially, the concentration is zero throughout the material: $c : (x, t < 0) = 0$. At $t = 0$, a constant concentration is applied at the feed side: $c_1 : (t \geq 0) = c_1^0$. Owing to this change of charge, a flow from the feed side to the permeate side starts and c_2 changes with time.

The flux at the permeate side was calculated [20] if $c_2 \approx 0$ and $c_2 \ll c_1$ for all t resulting in equation 2.24:

$$J(t) = \frac{Dc_1^0}{l} \left[1 + 2 \sum_{n=1}^{\infty} (-1)^n \exp\left(-\frac{Dn^2\pi^2 t}{l^2}\right) \right] \quad (2.24)$$

The steady state flux will then be:

$$J_{\infty} = \lim_{t \rightarrow \infty} J(t) = \frac{Dc_1^0}{l} \quad (2.25)$$

2.4.2 Atomistic Description

Structural defects such as dislocations, grain boundaries, internal and external surfaces must be taken into account in the study of diffusion. However it is common to find only a distinction between lattice and grain boundaries diffusion. This happens because it is experimentally more difficult to perform qualitative measurements on the other structures, leading to fewer quantitative experimental data.

Lattice Diffusion

Lattice diffusion takes place through the movement of point defects. The presence of different types of point defects gives rise to different mechanisms that may occur simultaneously.

The general mechanisms of diffusion in metals are described in [21] and graphically summarized in figure 2.4.

The interstitial mechanism is characterized by the jump from one interstitial site to the adjacent one. Such a movement or jump involves a considerable distortion of the lattice. Hence, this mechanism is only probable when the interstitial atom is smaller than the atoms on the

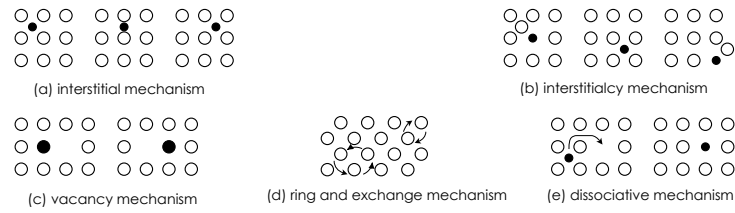


Figure 2.4: Mechanisms of diffusion [15]; in the case of hydrogen in metals only the interstitial, vacancy and dissociative were reported

normal lattice positions (e.g. H, C, N or O).

If the distortion during the jump becomes too large, the interstitialcy mechanism takes place. The interstitial atom will then push one of its neighbours on normal lattice sites onto another interstitial position and occupies the lattice site of the displaced atom itself.

The vacancy mechanism occurs if an atom on a normal lattice site jumps into an adjacent unoccupied lattice site. The movement of atoms ensues in the opposite direction of the vacancies which concentration increases with increasing temperature.

The dissociative mechanism is characterized by alternating atom jumps from vacancy to interstitial sites. This mechanism is predominant in small atomic diffusion.

In the case of hydrogen in metals, only the interstitial, vacancy, and dissociative diffusion were reported [22–24]. Fromm [24] even stated that only the interstitial site diffusion should be considered. Wipf [23] agreed that hydrogen exists mainly as an interstitial in metals, but also emphasized the importance of traps in the crystal.

Traps are formed by lattice defects, such as vacancies or dislocations, that interact attractively with the atom increasing the activation energy required for it to escape and therefore reducing the diffusivity. In fcc metals, due to the larger free volume, trap binding energies are relatively low. Therefore this trapping effect is not usually considered.

Grain Boundary Diffusion

As a general rule, lattice diffusion will tend to predominate at high temperature. With the decreasing temperature however, grain boundary diffusion becomes increasingly important. Grain boundaries are internal interfaces that represent sharp crystallographic orientation changes where the dominant diffusion mechanism is primarily a vacancy motion [22, 25]. Although the diffusion in grain boundaries is not fully understood, several publications agree in that it is much faster than in the lattices [26, 27]: ratios in the range of 8 - 100 can be found in the literature. It is also reported a generally lower activation energy in grain boundaries than in the crystal [25, 28, 29]. The following rule was established [29]:

$$\frac{H_G}{H_{Bo}} \approx 2 \quad (2.26)$$

where H_G and H_{Bo} are the diffusion activation energy in grains and grain boundaries respectively.

2.5 Permeation

2.5.1 Phenomenological Description

The permeation of gas through metals is a complex physicochemical process that includes:

1. adsorption,
2. dissociation on the metal surface (if its a molecular gas like hydrogen),
3. absorption from the surface to the metal,
4. diffusion due to the concentration gradient of the atomic hydrogen,
5. recombination and desorption of the molecular hydrogen on the metal surface.

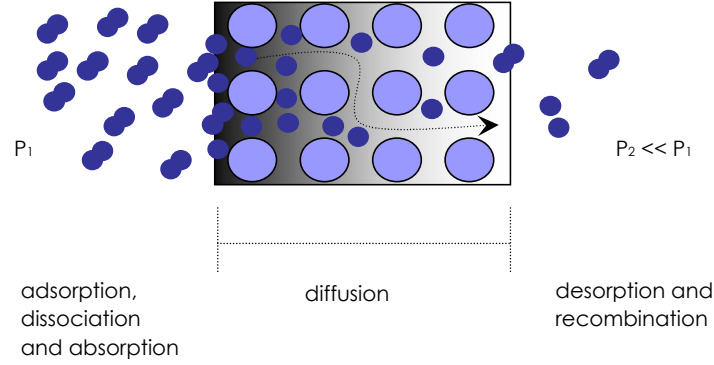


Figure 2.5: Schematic of the mechanism of permeation for two atomic gases

If the surface is clean and the surface reaction is sufficiently fast, the diffusion step is rate controlling in the hydrogen permeation process. If the permeation surface area is sufficiently large compared to the thickness, only one-dimensional diffusion normal to the surface is considered. A schematic representation of permeation of two atomic gases can be observed in figure 2.5.

When steady state diffusion is achieved, i.e. a constant concentration gradient is established in the specimen for an infinite time, J is expressed as J_∞ :

$$J_\infty = -\frac{D(c_2 - c_1)}{l} \quad (2.27)$$

where c_1 and c_2 are the hydrogen concentrations at the inlet and outlet surfaces respectively and l is the specimen thickness.

Using Sievert's law ($C = SP^{\frac{1}{2}}$), equation 2.27 takes form:

$$J_\infty = -\frac{DS(P_2^{\frac{1}{2}} - P_1^{\frac{1}{2}})}{l} \quad (2.28)$$

where P_1 and P_2 are the equilibrium hydrogen pressures at the inlet and outlet surfaces respectively.

In general $P_1 \gg P_2$ and DS is defined as the permeability:

$$\phi = DS \quad (2.29)$$

the permeability is also expressed by the Arrhenius equation 2.30

$$\phi = \phi_0 \exp\left(\frac{-H_\phi}{RT}\right) \quad (2.30)$$

where ϕ_0 is a temperature-independent material constant and $H_\phi = H_S + H_D$ is the permeation activation energy in J mol^{-1}

2.5.2 Experimental Determination of the Permeability

The majority of permeation measurements at high temperatures are performed using the transmission method. The gas is applied to the feed side of a membrane. The flux on the permeate side is measured in either a flowing stream (constant P) also called dynamic regime; or a closed chamber (constant V) and usually named static regime. Due to hydrogen high conductivity and the fact that the measurement is performed at high temperatures, the dynamic regime is employed in this work.

The permeate side of the specimen is considered to be quasi-stationary, $\partial P/\partial t \approx 0$. Presuming that no leakage exists, the principle of mass conservation requires that the sum of the gas flows owing to permeation, outgassing and pumping to be zero:

$$-Q_T + Q_\phi + Q_O = 0 \quad (2.31)$$

This equation states that the total gas throughput, Q_T , consists of two parts: i) the gas led into the chamber, Q_ϕ and ii) the gas coming into the chamber due to outgassing from the walls and through the vacuum seals, Q_O . This outgassing is the reason why the base pressure is never zero.

The typical procedure of the permeation measurement in the dynamic regime is:

- at $t < 0$, the gas concentration of the sample is near zero.
- at $t = 0$, a constant pressure P_1 is applied at the feed side.
- the permeate side is permanently kept at HV, and the flux or flow are recorded.

Presuming a homogeneous material and no kinetics in the sorption process, the permeability can be calculated substituting equation 2.29 in 2.28 and rearranging the result:

$$\phi = \frac{J_\infty l}{P_1^{\frac{1}{2}}} \quad (2.32)$$

Equation 2.32 is valid for stainless steels, if the feed pressures are greater than 10 Pa and less than 5×10^7 Pa, and/or the temperature is less than 1373 K [19].

2.6 Factors that Influence the Permeability

2.6.1 Cold Working, Heat Treatments and Alloying Elements

In general, no significant influence of cold working, heat treatment and alloy composition are noticed on the hydrogen permeabilities and diffusivities [30]. However some studies found that:

- Annealing treatment resulting in increased grain size decreased the diffusivity, possible due to the longer hydrogen transport path through the grains and less contribution of fast diffusion paths [31].
- Alloying elements such as aluminium, silicon, titanium, chromium, manganese, niobium and vanadium may reduce the permeability by acting as trap sites [30, 32].

2.6.2 Surface Condition

Many studies [30, 33, 34] mention the formation, at the surface of the SS specimens, of thin protective films, consisting mostly of chromia (Cr_2O_3) [35], with thicknesses ranging of 10-160 Å [34]. Evidence that these films development occurred while testing was provided by a post

examination of the measured specimens through interference colour matching [34].

These films were thought to contribute to a strong reduction of the diffusivity and permeability, sometimes in two or three orders of magnitude [19, 36]. It was also reported its presence lead to a change in the surface kinetics causing the lost of the square root dependence of pressure and flux.

The growth of the films was attributed to the elevated temperature exposure to oxygen, water and other impurities retained on the surfaces of the test apparatus. Its formation was reported to occur even after evacuation to reasonable levels at room temperature [34].

Formation of a Cr_2O_3 layer

The oxidation of Cr is thermodynamically favourable at pressures deep in the UHV range at a $T < 873$ K. In a Cr containing alloy however a protective Cr_2O_3 layer is built up above a critical concentration of Cr which is function of T and oxygen partial pressure [37]. At high temperatures ($T > 1273\text{K}$) and laboratory air, the minimum bulk concentration of Cr necessary to form a protective oxide layer is reported to be in the range 17-20 wt.% [38]. The deformation of the steel's surface can however dislocate this range to lower values. The initial oxidation of a 18% chromium containing ASS can then be divided into 4 main stages:

1. adsorption of O_2 gas on the surface,
2. formation of individual oxide nuclei,
3. lateral growth of the oxide nuclei to form a continuous oxide film,
4. further growth of the oxide film normal to the surface.

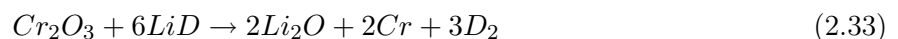
The oxygen is transported inwards from the layer/ gas and chromium outwards from the metal/ layer interface. During the initial layer formation only the last transport process is significant. In this initial period the concentration of Cr at the interface decreases. For further growth, Cr must be supplied by diffusion, what may limit the oxidation rate. At temperatures below 1273 K the diffusion process occurs mainly along grain boundaries. In these conditions, Cr supply is generally not sufficiently fast. Therefore Cr depletion below the layer persists for a considerable time period and prevents further growth of the oxide layer. In the case of fine grained or cold worked materials, the formation of a chromia layer is enhanced because surface imperfections constitute fast diffusion paths and preferential nucleation sites [37, 38].

Control of the Surface Condition

Several ways of reducing the effects of the oxide layers are reported in literature.

One way is electroplating the sample with palladium that possesses an exclusive perm-selectivity to hydrogen. The standard procedure is, after polishing, electroplate the samples, at a small current (about 1 mA), in a bath with an aqueous solution of palladium chloride, dibasic ammonium phosphate and ammonium chloride. The coatings then obtained are about $0,1 \mu\text{m}$ thick. More details on this can be found on reference [30].

The surface effects can also be controlled by placing grinded $250 \mu\text{m}$ LiD powders in the specimens before evacuation and backfilling the chamber with deuterium [34]. The powders cause the reduction of the chromia film through the following reaction:



Similar reaction occurs in the reduction of iron and nickel oxides. Hydrogen exposure can also reduce the oxide layer through the reaction:



However such occurrence is only reported [39] with a continuous removal of water vapour from the reaction zone and at temperatures above 1300 K.

The possibility of formation of protective oxide films, requires a careful analysis of the results. If the oxide formation at the surface is prevented, factors that contribute to a higher diffusivity also lead to higher permeability values. However if these surface effects are not controlled, a higher diffusivity might lead to a reduction on the permeability.

Chapter 3

Materials and Methods

3.1 Initial and Final Permeation Measurement Device Description

Both initial and final permeation measurement devices (PMD) can be subdivided into measuring chamber (highlighted in figure 3.1), pumping system, gas supply and measuring/control system.

The chambers are constituted by a 2 mm thick stainless steel recipient with the dimensions 620x150mm. CF connections are placed both in the top and bottom and at the middle of its length, where a valve, that allows or disrupts the flow passage to the measuring system, is placed.

The sample is positioned in a CF Blank flange screwed at the top of the recipient. At the bottom is positioned another CF Blank flange with three openings: one connected through a valve to the vacuum system. In the remaining two are placed feedthroughs that establish connections from the heating system and temperature sensor to the control system and power supply. The upper valves connect the sample to the pumping system, which keeps the vacuum inside the sample and to a H₂ gas supply. The considerable volume of the last has the function of preventing a sudden decrease of the gas pressure during the experiment. From the four chambers initially built, only two could be used simultaneously.

The final permeation measurement device is schematically presented in figure 3.2.

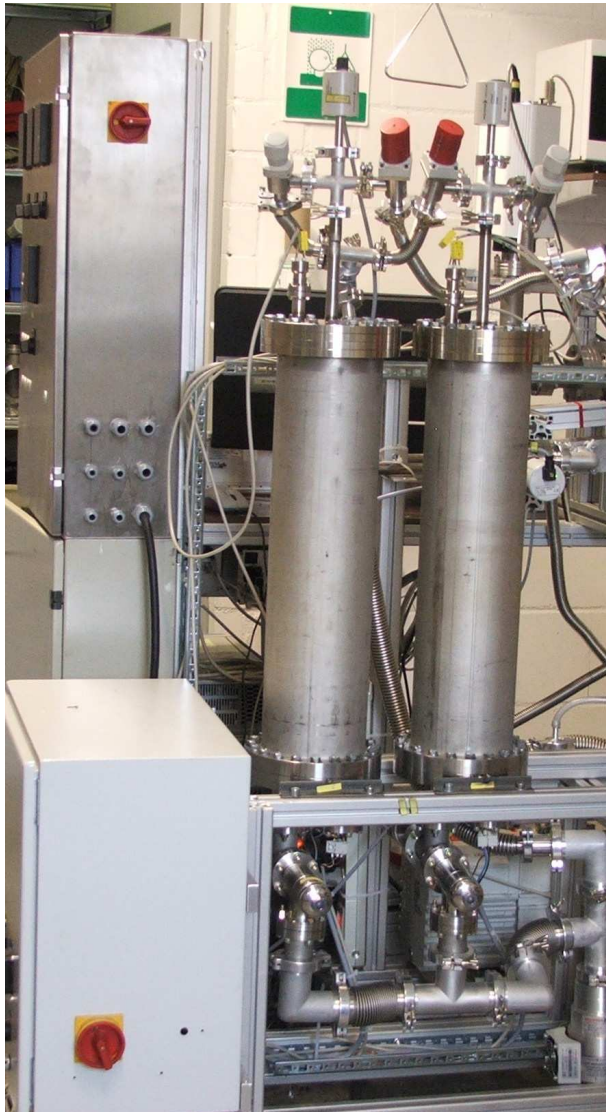


Figure 3.1: Measuring chambers in the final permeation device; consist of 620×150 mm recipients. The bottom valves connect the chambers to the pumping system, the upper valves connect the sample to the pumping system and gas supply. Capacitance diaphragm gauges measure the gas pressure inside the sample.

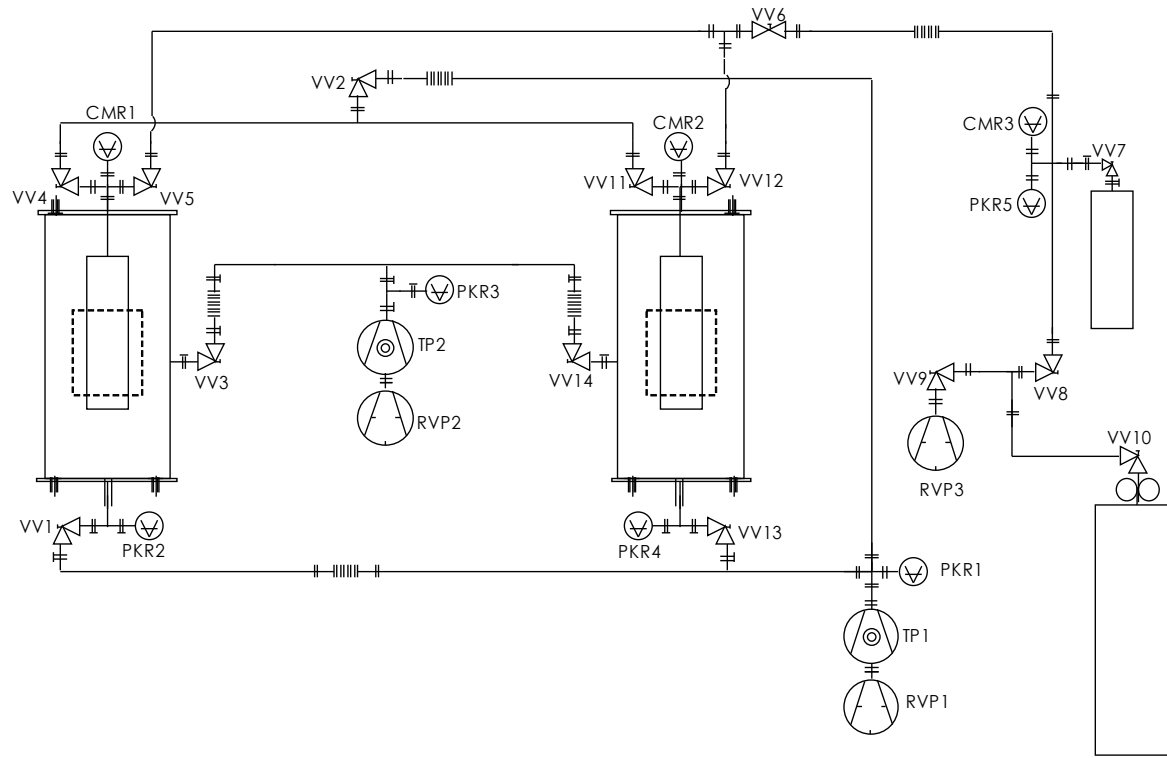


Figure 3.2: Final Permeation Measurement Device Scheme; Chambers 1 (left) and 2 (right), diaphragm (CMR) and full range (PKR) gauges, turbo-molecular (TP) and rotary vane pumps (RVP), hydrogen supply, reservoir, flanges and feedthroughs positioning

3.1.1 Vacuum Components

Types of Flanges

The vacuum components used have KF or CF (ConFlat) flanges.

The KF connection is made through an elastomer seal and a tension ring.

The CF flange connection can be made by gold, silver or copper rings depending how low is the vacuum level to be achieved (gold is the lowest followed by silver). Since we work only in the HV level, for economic reasons copper rings were used.

This type of flange is used in HV and UHV technology because of its low leak and desorption rates as well as its compatibility to high temperatures. Due to these characteristics, CF connections were placed in the recipient and in the parts of the device connected to the measurement system.

Vacuum Pumps

The pumping systems consisted of a turbomolecular pump (TP) connected to the inlet of a rotary vane pump (RVP). A TP basically compresses the flow in a multitude of vertical stages. Each

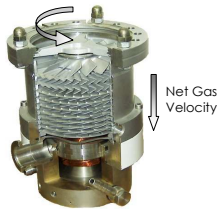


Figure 3.3: Turbo pump section [40]; direction of the flow and blade rotation. The rotor and stator possess a number of angled blades mounted in series.

stage is constituted by: i) a rotor driven by a motor and automatically controlled by an external frequency converter; ii) a fixed stator. Both components have a number of angled blades pairs mounted in series with a rough surface to prevent the occurrence of reflection.

The compression process can be summarized by the following:

1. the incoming gas molecules gain mechanical energy through collision with the lower side of the blades,
2. most scattered molecules are lead downwards to the transfer holes in the stator due to the surface direction of the blade in contact region,
3. the molecules enter the next stage and again collide with the rotor blades surface which now have shorter radial spans,
4. the process continues until gas molecules go outwards through the exhaust.

When selecting a TP two main characteristics must be taken into account: the pumping speed that depends on the type of gas [16] and the maximum compression ratio.

The compression ratio, K , is a characteristic that limits the minimum pressure a device can reach. Can be obtained through equation 3.1.

$$K = \frac{P_{outlet}}{P_{intake}} \quad (3.1)$$

When P_{intake} is low enough that $K = K_{max}$, the pump cannot bring the pressure down anymore. This limit on the compression ratio comes from the fact that when there are not many molecules left in the chamber, the probability of a molecule coming back from the outlet to the intake is comparable to the probability of a molecule being driven toward the outlet by the pump. To increase the probability of a molecule being pumped, the system has to be subjected

to higher rotational speed. This can only be attained by changing the TP for a faster one.

At atmospheric pressure molecules move in bulk. Most TPs can not work at this pressure range because the force exerted by a blade on a molecule is not significant compared to the collisions between the molecules, as a result, the general flow remains unaffected. A rotary vane pump (RVP) has to remove gases, before the TP is turned on, down to the molecular flow range (about 0,1 Pa), where molecules are relatively free and, to a good approximation, do not interact with each other.

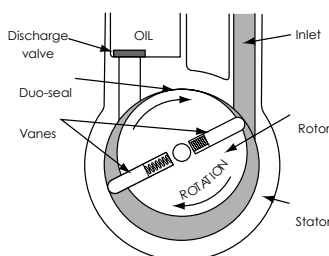


Figure 3.4: Rotary Vane Pump schematic representation [41]; the inlet pressure causes the rotation of the vanes and the gas is forced out through the discharge valve

A schematic representation of a RVP is shown in figure 3.4. It has a rotor whose vanes rotate inside of a cavity due to springs and centrifugal force. On the intake side of the pump, the vane chambers are increasing in volume which is filled with gas forced in by the inlet pressure. On the discharge side of the pump, the vane chambers are decreasing in volume, forcing gas out by the oil sealed discharge valve.

The oil reservoir of the rotary vane pump serves the purpose of lubrication and sealing, and also to fill dead spaces and slots. It removes the heat of gas compression, and provides a seal between rotor and cavity. The gas ballast valve admits a defined quantity of gas previously to the compression process. This prevents the condensation of vapours inside the cavity. Otherwise this would lead to emulsification of the condensed vapour with the pump oil causing the decrease of the oils lubrication qualities and ultimately the seizure of the pump. When a RVP is operated close to ultimate pressure at high temperature, back diffusion might occur. In these conditions there is a dynamic equilibrium between the transported gas flow and oil vapour pressure that results on the migration of the oil back to the vacuum line. That migration occurs in the opposite direction of the pumped flow which is, in our case, the outlet of the TP. Back diffusion can be avoided using condensation traps.

The final device had two pumping systems. One was used to evacuate both recipient and sample. The second was used to prevent the accumulation of hydrogen in the chamber and therefore enable the measurement. Additionally a rotary vane pump was used to pump the hydrogen supply. The position of the used pumps in figure 3.2 and respective characteristics are shown in tables 3.1 and 3.2.

Table 3.1: Turbomolecular pump characteristics [42], pumping speed in l/s and compression ration

Designation	Model	s_{H_2}	s_{N_2}	$K_{max}N_2$
TP2	Pfeiffer TPD 011 TC100	3,7	10	3×10^2
TP1	Pfeiffer TMH 071	32	59	$>10^5$

Table 3.2: Rotary Vane Pump models, pumping speed for nitrogen (in m^3/s) and ultimate pressure (in mbar) [42], [43]

Designation	Model	$s \text{ N}_2$	$P_{ultimate}$
RVP3	Primary Pfeiffer DUO 5M	6	2×10^{-2}
RVP1	Primary Pfeiffer DUO 20M	20	1×10^{-2}
RVP2	Oerlikon TRIVAC D2,5 E	2,5	3×10^{-2}

3.1.2 Heating System

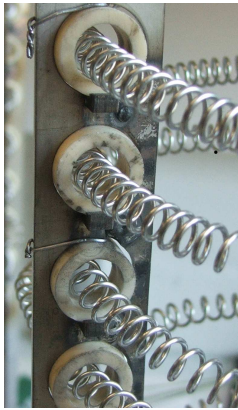


Figure 3.5: Isolation between the heating system and heating wire; was achieved recurring to ceramic rings fixed with metal clammers (positioned under the ceramic rings) and zinc free wire (above the ceramic rings)

The initial heating system (HS), shown in the left side of figure 3.6, consisted of a spiral CrNi8020 heating wire surrounding a stainless steel metal skeleton. The isolation between heating wire and skeleton was made through ceramic (alumina) rings fixed with a metal clammer and high temperature resistant, zinc free, wire (see figure 3.5).

The metal skeleton comprised 4 supports welded on a metal base. The HS was divided into 3 heating zones (shown in figure 3.6) distanced 10 mm of the sample: two outer (blue and pink rectangles) 60 mm and a central (green) 80 mm long. The heating zones operated at 60V and delivered 500W. The three heating zones were surrounded by stainless steel parts that altogether constituted the radiation shield. The central part was 124 mm long and had 3 holes where the controlling temperature sensors were placed. Both top and bottom parts had the function of keeping the welding seals at the ends of the sample as cold as possible and therefore minimize its contribution to the hydrogen permeation.

The heating wire was cut into sections with a 7Ω resistance, stretched and placed in the ceramic rings.

The present HS, shown in the right side of figure 3.6, consists on two parts (in blue) controlled independently, with the dimensions 81 x 122 mm inserted in a metallic support.

The spiral heating wire is covered with quartz and therefore completely isolated from the skeleton. The operating voltage and power are 230 V and 1300 W respectively. The radiation shield is constituted by 0,8 mm thick 1.4301 stainless steel easily removable parts: two discs at top and bottom and a metallic cylinder in the centre.

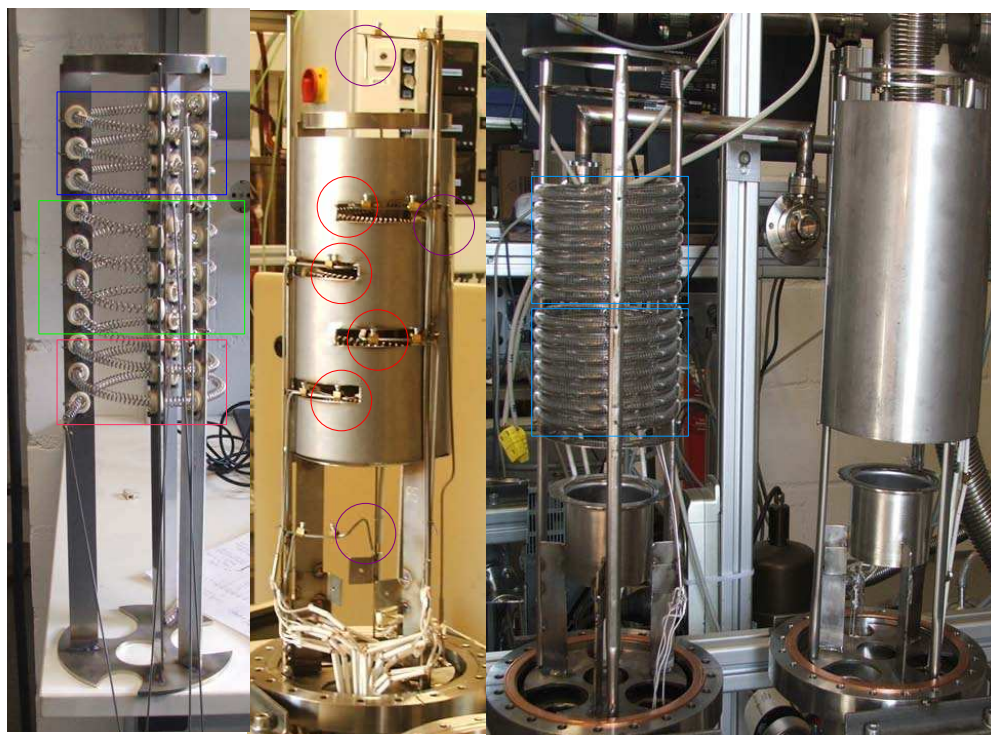


Figure 3.6: Initial and final heating system; initial heating system consisted on a heating wire surrounding a metal skeleton enclosed by a radiation shield. Rectangles represent the heating zones and circles the sensor position. The final heating system consists on a glass spiral wire in a metal skeleton surrounded by a radiation shield. The metallic cylinder in the bottom is used to centre the sample.

3.1.3 Temperature Regulation, Control and Data Recorders

The control of the first HS along with the temperature data recording, was performed by hardware and software interfaces: National Instruments Fieldpoint modules controlled by a LabVIEW program.

The automatized control of the system was achieved through the use of a proportional-integral-derivative controller (PID) incorporated in the LabView program.

Table 3.3: Effects on increasing Parameters [44]

Parameter	Rise Time	Overshoot	Settling Time	Error
P	Decrease	Increase	Small Change	Decrease
I	Decrease	Increase	Increase	Eliminate
D	Small Decrease	Decrease	Decrease	none

The PID controller controls the process variable through an algorithm that (1) determines the error between a measured value and the desired set point (2) outputs the corrective action and adjusts the process accordingly. The algorithm involves three separate parameters:

- the proportional value, P, that determines the reaction to the current error,
- the integral, I, which determines the reaction based on the sum of recent errors,
- the derivative, D, that determines the reaction to the rate at which the error has been changing.

The weighted sum of these three actions is converted usually to time and used to adjust the process. In our case the temperature was regulated by power on and off the heating system supply in the determined time period.

To find the optimal temperature loop performance is necessary to tune the PID parameters. Taking table 3.3 as a starting point, the tuning procedure was the follow:

1. Input a small temperature and reduce the Overshoot by reducing the value of P and I and increasing the value of D.
2. Input a higher temperature and follow the same procedure until the working temperature is reached.
3. Change the values of I and D until the stability of the loop is satisfactory.

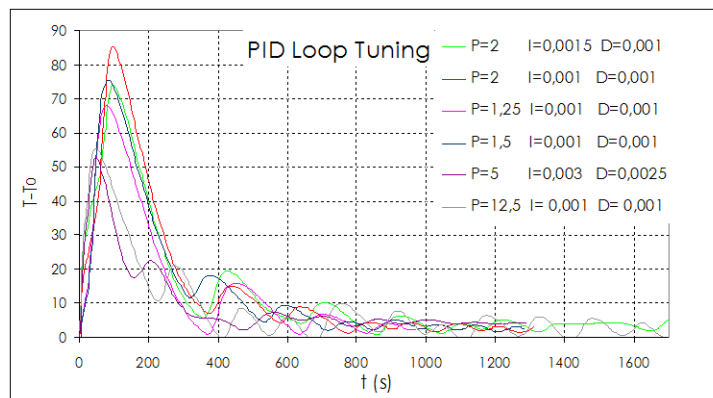


Figure 3.7: PID loop tuning temperature curves; effect of changing parameters on temperature; T_0 and T corresponds to initial and final temperature and t is the time in seconds

Figure 3.7 shows the different temperature curves obtained by varying the P, I and D parameters.

The final result was a temperature variation with time as it is shown in figure 3.8

The new control system consists of a compact microprocessor controller with a PID structure and automatic tuning used along with a thyristor, to reduce the HS power. The resultant measurement temperature curve is shown in figure 3.9.

In the final configuration, the Fieldpoint modules along with the LabView interface were used only for temperature and pressure data recording. The series of modules consisted of a network

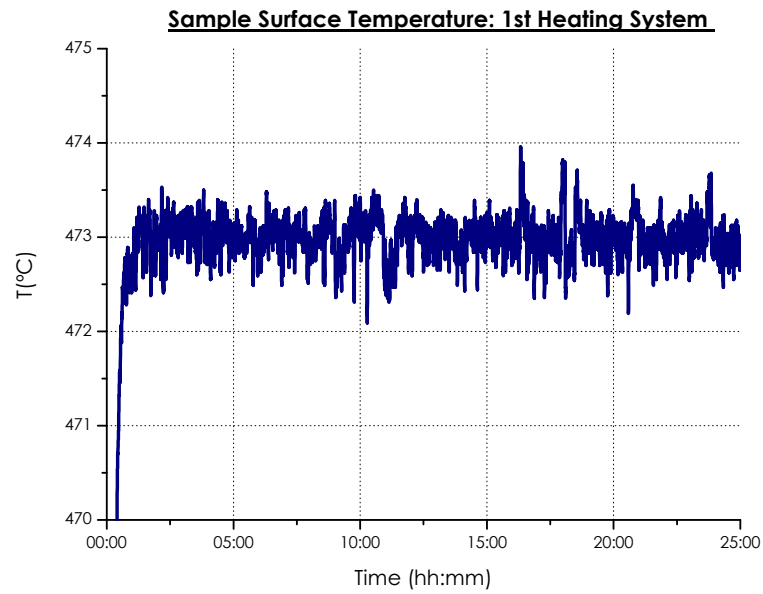


Figure 3.8: Samples surface temperature curve for the initial heating system; difference of 2°C between the higher and lower point

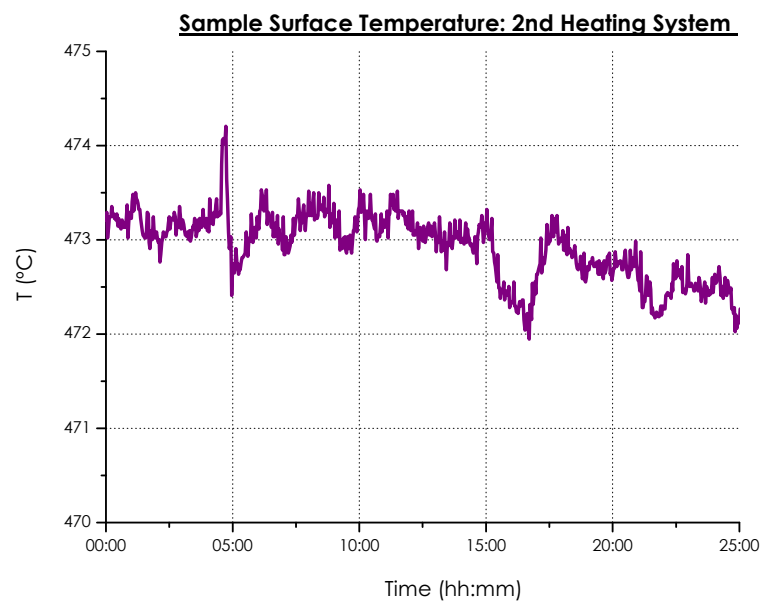


Figure 3.9: Samples surface temperature curve for the late heating system; difference of approximately 2,5°C between the higher and lower point

module (FP-1601), a power supply (FP-PS-4) and a digital output (FP-DO-401) modules. Modules specially conceived to work with PRT (FP-RTD-124 with 32 channels) and to enable the pressure measurements, (FP-AI-110 with 5 channels) were also used.

3.1.4 Measuring Components

Temperature Sensors

The temperature sensors used were platinum resistance thermometers (PRT) more specifically PT100 (at 0°C they exhibit a 100Ω resistance) that offer excellent performance in the temperature range from -200 to +850 °C.

The sensors are made from platinum due to its linear resistance-temperature relationship and its chemical inertness. The platinum wire is encapsulated in a sheath and connected to two copper wires. The copper wires are kept from contacting by a non vacuum stable ceramic insulator. Outside the sheath this isolation is maintained by a fiberglass cover and ceramic cylinders. Whenever the two wires contact the sensor stops working and the system displays a value of T=850. This happened during the course of this work but in most cases only in the experimental working range.

The temperature sensors were first positioned in 8 different locations (see figure 3.6): 2 sensors in the welding seals, 2 in the central part of the radiation shield and 6 in the sample. From these, 4 (in red) were used to control the heating system: 2 at the middle and the remaining 2 in each outer heating zone. To assure its contact with the surface of the sample, the sensors were attached to high temperature resistant coils made of Inconel.

In the new set up the heating parts control was performed separately by one sensor distanced 10 mm from the sample and positioned in the middle of each heating part. Additionally one sensor was wired to the sample to allow the registry and detection of irregular temperature conditions.

Mass Spectrometer

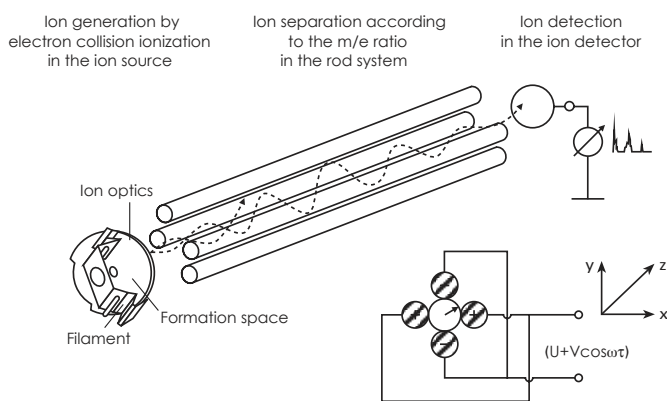


Figure 3.10: Functioning Principle of QMS 200 [45]; ions with a particular mass/charge ratio are lead by a high electric quadrupole field to the ion detector

Initially all the measurements were performed by a quadrupole mass spectrometer Pfeiffer QMS 200. This device is equipped with a 4 parallel metal rod system (figure 3.10), that creates a high frequency electric quadrupole field with a voltage $V\cos\omega\tau$, a superimposed direct voltage U and radius r_0 .

The neutral particles arriving in the ionizing space are ionized by the filaments of the ion source. The ion source is usually protected by a full range gauge that shuts it down in case a pressure higher than 1×10^{-4} mbar is reached.

The ions, under the influence of the high frequency field, oscillate perpendicularly to the field axis. For certain values of U , V , ω and r_0 only ions with a particular ratio m/e can pass through the separating field and reach the ion detector. The trajectory of ions with a different mass/charge ratio is unstable resulting in its collision with the rods. In this way the ions are rejected by the quadrupole field and a mass/charge ratio scanning is achieved. Different mass/charge ratios can

be obtained by varying the frequency ($m/e \approx 1/\omega^2$) or voltage ($m/e \approx V$).

In this work the measurement type used was the multiple ion detection (MID) mode. The measured intensities were displayed as a function of time as it is shown in figure 3.11.

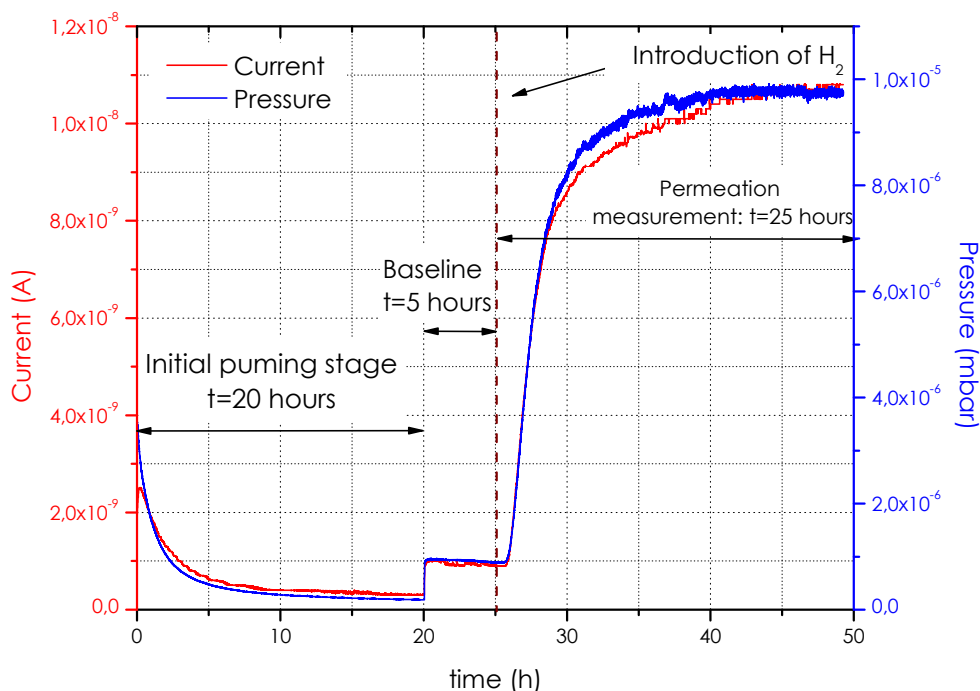


Figure 3.11: QMS measurement profile; Current (red) and Pressure (blue) curves, and stage identification

The calibration of the device previous to the experiment is necessary to convert the obtained values of current into gas amount.

The calibration method used in the former work [46] consisted in measuring the flow that passed through a removable capillary with known diameter and length, and compare it to the obtained current.

First the pressure growth rate (mbar/s) was measured: hydrogen was fed into the capillary that led the gas into a closed chamber (in HV) with a known volume. The pressure increase was registered and the flow obtained through the slope of the pressure vs time line. The capillary was then placed between the gas supply and a special sample, with two holes in the ends, in the PMD. After obtaining the baseline, the gas was lead to the holes of the sample and finally pumped by the QMS. After obtaining a constant current, the supply was interrupted and the procedure repeated several times for each capillar. The conversion of current into flow and current was made through the linear regression of the flow vs current graphic.

Due to the degradation of the capillaries used and the impossibility of applying this method at the beginning of each experiment, calibration test leaks, to be attached directly to the QMS, were ordered.

The measurements performed until this point indicated that the partial amount of elements other than hydrogen was not significant during the course of the experiment. The permeation tests

then proceed but now recurring to pressure measurements.

Pressure Gauges

Two types of pressure gauges were used: a capacitance diaphragm and full range gauge.

Capacitance diaphragm gauges are used from atmospheric pressure to 0,1 Pa.

The pressure is measured through the change in capacitance of a plate capacitor constituted by two electrodes: one fixed and the diaphragm. When the diaphragm deflects, due to the variation of pressure, the distance between the two electrodes changes and the capacitance is altered. To ensure sufficient deflection at different pressure levels, diaphragms of several thicknesses are used. In this work capacitance gauges CMR 261 from Pfeiffer, with 0,2% accuracy, measured the input pressure of hydrogen.

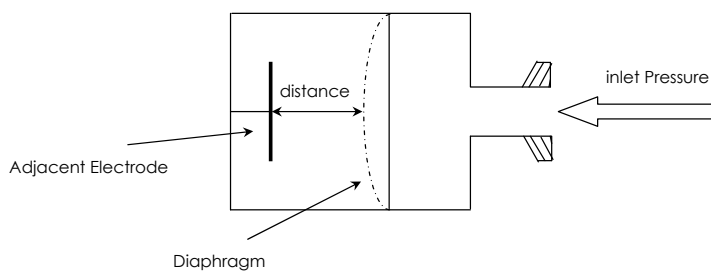


Figure 3.12: Diaphragm capacitive gauges working principle; the inlet pressure causes the deflection of the diaphragm and the capacitance of the system is altered

The full range gauge consists of Pirani and cold cathode measurement systems combined in such a way to present an uniform behaviour.

In a Pirani system (figure 3.13), the pressure is measured through the heat loss of a suspended

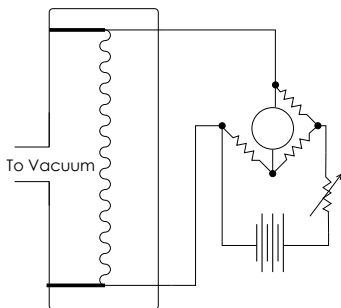


Figure 3.13: Pirani Circuit [47]; collision of particles with a metal filament result on the variation of its electrical resistance

metal filament, result of the collision of gas molecules. If the gas pressure decreases, the number of molecules present will fall proportionately and the wire temperature increases due to the reduced cooling effect. This increase will then result on the variation of the electrical resistance of the wire. In many systems the pressure can also be determined by the measurement of the required current to maintain the wire at a constant temperature.

At pressures lower than 1 Pa the Pirani system can no longer measure and the cold cathode measurement circuit is activated.

A cold cathode or Penning system (figure 3.14) contains two unheated electrodes: a cathode and an anode. Between these two, a so-called cold discharge is initiated by means of a d.c. voltage (of around 2 kV) and maintained by a magnetic field. The magnetic field lines of force cross the electric field lines, confining the electrons to a spiral path. The electrons collide with the gas particles that become positive or negative charged and move to the corresponding electrodes. This results in a pressure and gas dependent discharge current. This method is reliable only

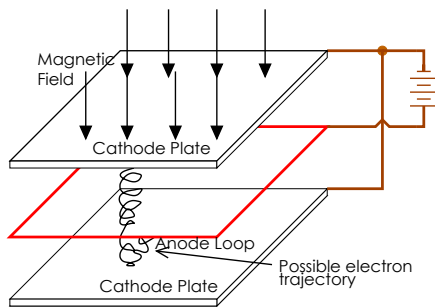


Figure 3.14: Penning Gauge [47]; electrons confined in a spiral path ionize gas particles that are directed to the corresponding electrode

for measuring ranges below 1 Pa. Above this level the discharge changes to a glow discharge with intense light output in which the current (at constant voltage) is scarcely dependent on the pressure.

This type of system presents three outstanding advantages: is the least expensive, insensitive to sudden admission of air and vibrations and easy to operate. The big disadvantages are its high susceptibility to contamination, resultant either from the sputtering of the cathode material by the ions produced in the discharge and the continuous operation in the range of 10^{-2} - 1 Pa.

The full range gauges used were Pfeiffer PKR 261 models which present reproducibility and accuracy of respectively 5 and 30% of the measured value in the range 1×10^{-6} - 1×10^4 Pa.

3.2 Problems Faced and Respective Resolution

Most significant problems that occurred in the course of this work are displayed in the cause effect diagram of figure 3.15.

The green items represent problems that were permanently resolved. The remaining are situations that were minimized but may again occur.

Observing the diagram one can state that the biggest achievements were a reliable heating system and a reproducible temperature control. The development of the sample preparation procedure also allowed to resolve several experimental errors. In the remaining categories the encountered problems were temporarily resolved and detection methods (such as the use of extra pressure gauges) were enabled.

3.2.1 Heating System

A situation that occurred frequently in the initial PMD was the conduction of current between the heating wire and the HS metallic components (radiation shield and metallic skeleton). This would happen during the experiment and resulted in the shut down of the PMD by the safety fuse. These short circuits were attributed to the heating wire expansion and/or vibration which would then contact the metallic clammers and radiation shield. Tracking these contact points was extremely difficult (sometimes even required the radiation shield to be saw) and the solution, consisting of the placement of ceramic parts, was temporary since they were soon displaced due to heating wire's expansion/vibration.

Short-circuits become even more frequent when one of the ceramic rings, incorporated in the metal skeleton broke. Its replacement was not possible and the ceramic parts placed around the heating wire wouldn't remain longer in the required position. At this point we start to look for alternatives since it had become clear that it was not feasible to work with this heating system. The confirmation of this assumption came with the break of the heating wire probably as a result of the stress points developed in the stretching process.

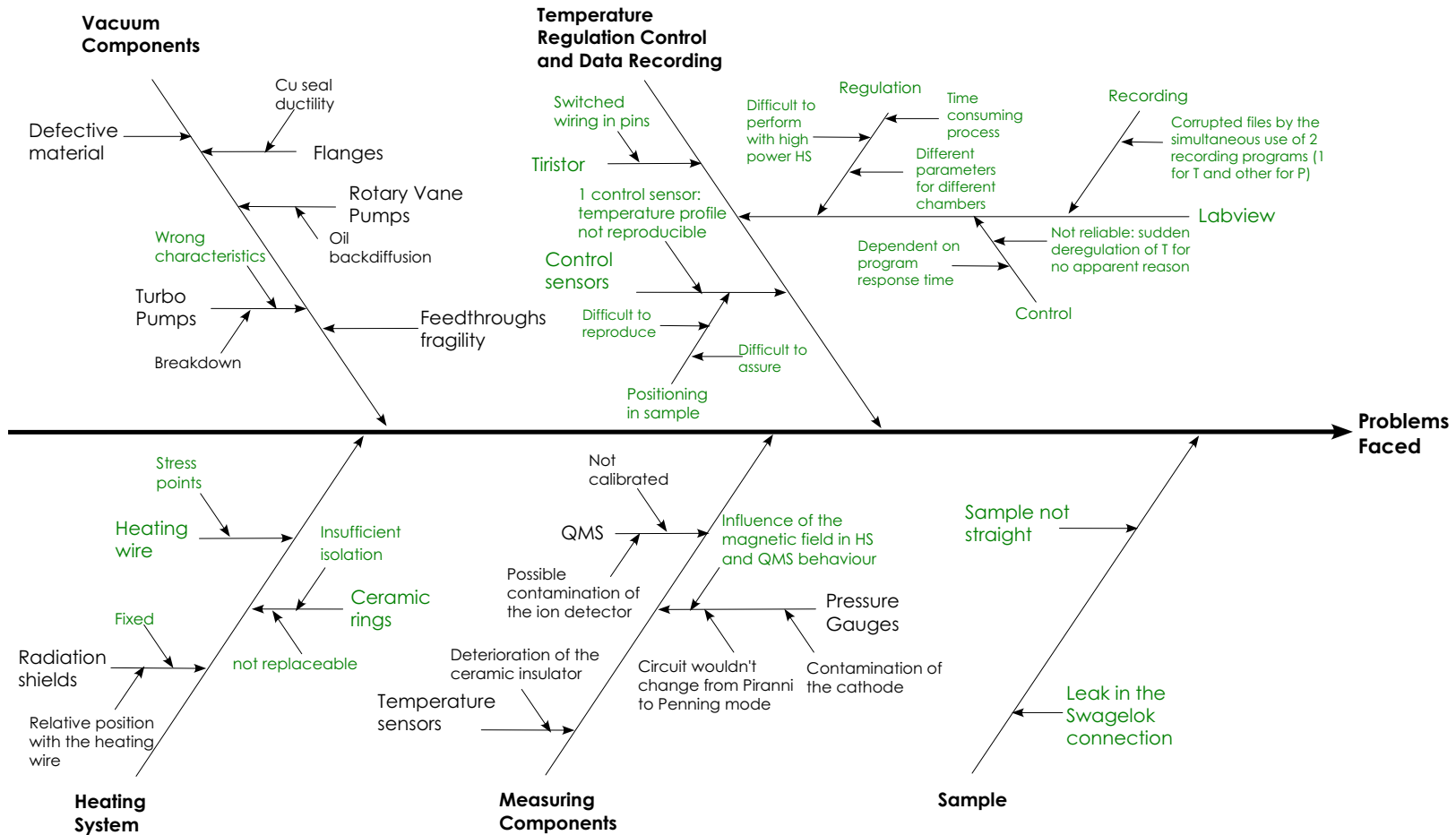


Figure 3.15: Cause effect diagram of the main problems faced

With the new heating system short circuits may occasionally occur but due to the isolation provided by the glass covering, the amount of possible contact points was strongly reduced. The few remaining can be easily detected and prevented since the radiation shield is easily removable.

3.2.2 Temperature Regulation, Control and Data Recording

LabView Limitations

The temperature control and recording was initially performed exclusively by a LabView interface. This software for simple procedures is quite good, however its use revealed not to be advisable for a simultaneous automated control of at least 4 temperatures. The program used was heavy and its performance could be affected by a change in the computers CPU utilization. This might explain the sudden temperature deregulation detected more than once.

The tuning of the automate parameters was painfully achieved for one heating system. Nonetheless this process was not only time consuming but had to be repeated every time the measurement temperature would change.

With the microprocessor controller the tuning was automatic and only one situation of temperature deregulation was observed. Since there was no obscure software in between, soon the source (switched wiring in the thyristor) was found.

A LabView program is currently used only to register the temperature and pressure data.

Number of Sensors and Positioning

The higher level of reproducibility within trials was also achieved by the definition of the optimal position and number of the controlling sensors.

The temperature control at the surface of the sample was initially guaranteed with the assistance of Inconel coils which assured the sensors positioning. However with the introduction of the sample, the coils would deteriorate and after a few runs was no longer possible to control the sensors position and subsequently the temperature profile in the experiment. The use of the coils was then discarded and in the new HS the control sensors were wired at the surface of the sample. Yet after the sample has been removed of the chamber, it would be often verified that the sensor positioning would have changed. It was not possible to know if this had occurred in introduction, withdraw or during the experiment as a consequence of expansion of the connecting wire. To minimize the temperature variation within the several trials, the control should be performed in such position that wouldn't vary with the samples introduction/removal. The sensors were then positioned 10 mm away from the sample.

The need to simplify the control of the heating system and the observation of some situations where the sensors had stopped working lead to the reduction of the number of control sensors initially used (4). First only one sensor positioned between the two heating parts was used to control the second HS. However the two registry sensors positioned in the sample indicated that the two heating parts would behave differently from one trial to another (see figure 3.16). For this reason the two heating parts were ultimately controlled separately by one sensor at their middle position (see sensor relative positioning in figures 3.22 and 3.23).

3.2.3 Sample

Two situations related to the sample condition also occurred in the beginning. The first was the leakage of hydrogen through the connection between the sample and hydrogen tube. To detect this situation a leak test was included in the experimental procedure previously to the probe introduction in the chamber. The second was the angle between the hydrogen tube and the steel covers sometimes differed from 90 degrees. This could be due to a bad cut, defective welding seam

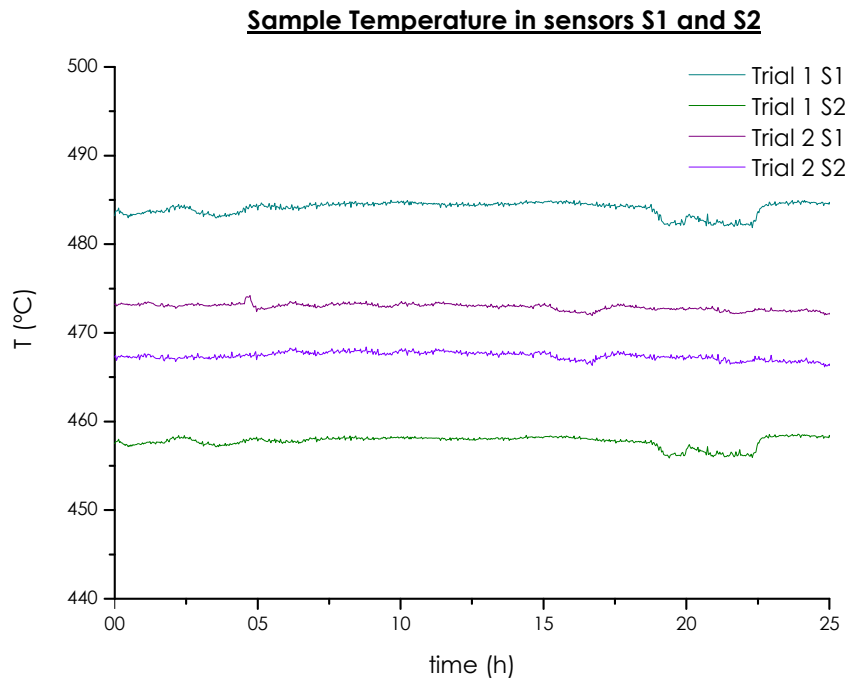


Figure 3.16: Behaviour of the heating parts in consecutive trials; S1 and S2 in positions 190 and 210 mm (relative positions in figures 3.23 and 3.22) the sample wasn't removed from the chamber between trials

or a hydrogen tube slightly bended. A water mark then started to be used to verify whether the probe was straight before the introduction in the device.

3.2.4 Vacuum Components

Defective Material

In the initial pumping stage is possible to infer the presence of leaks through the observation of the value of pressure at the gauge PKR1 (if it won't go lower than 1×10^{-4} mbar). Their exact location can be efficiently perceived by performing a helium leak test.

Common causes for leaks are deficient bonding between CF flanges, resultant of Cu rings deformed in the connection, or the presence of other defective material (such as valves, tubing, bad welding seams in flanges and tension rings).

Other issue within the HV material category that should be outlined is the fragility of the connection between the copper wires and feedthroughs. This situation is a setback especially because it is through these connections that short circuits are verified before closing the chamber.

Problems with Pumps

One of the problems verified was the presence of oil in tubing and TPs due to oil back diffusion in the RVP. This situation usually doesn't lead to the TP breakdown but decreases its rotation speed and thus its performance. Usually the presence of oil can be indicated by the reduction of the required time for the rotor to stop after the shut down of the pump. Since oil back diffusion

can seriously compromise the integrity the QMS, a condensation trap was used in the RVP connected to its TP. In the new device oil back diffusion can also affect the measurement results however it can be prevented if the measurement TP is always kept running.

The TP in which oil was detected was replaced by other TP with a lower compression ratio that wouldn't assure the required vacuum level leading to the coarse oxidation of the sample during the experiment.

The TPs breakdown due to exposure to atmospheric pressure, also occurred in several occasions. Its sources were usually deficiently closed valves, leaks and operating errors (such as opening the wrong valve). If this error occurs often may lead to the irreversible damage of the TP.

3.2.5 Measuring Components

QMS observed problems

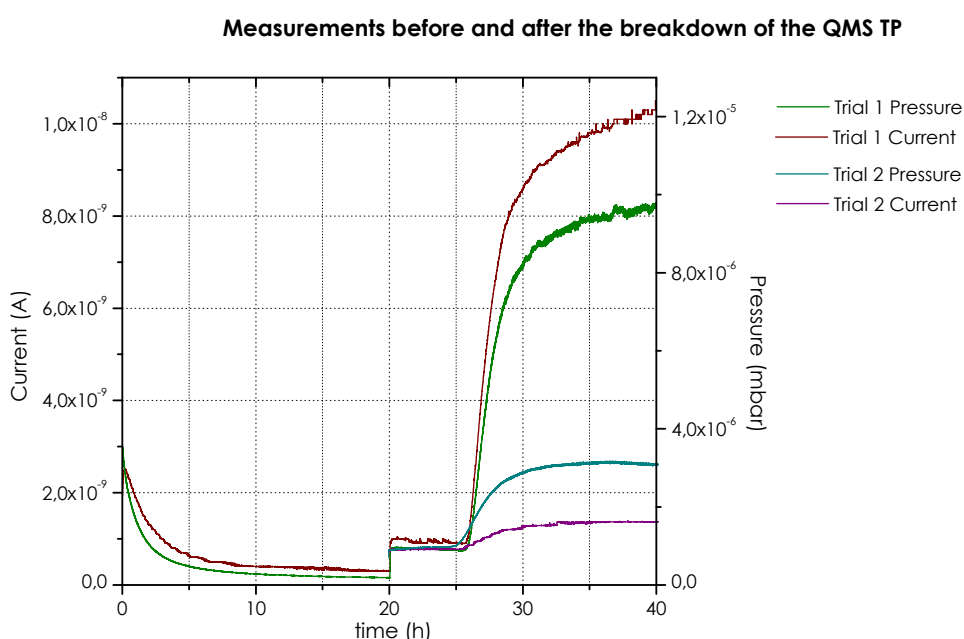


Figure 3.17: Influence of the TP breakdown in the measurement results; measurements in the same sample where trial 1 was performed previously to the TP breakdown and trial 2 after its repair

The incapability of obtaining quantitative values is problematic especially when there is a change in the experimental conditions. This was observed when the QMS turbopump broke down. After its repair the pumping speed had changed and measurements in a previously tested sample delivered completely different current values (see figure 3.17). Thus all the results obtained so far lost their significance.

The contamination of the ion detector also took place. In this case, for different trials for the same sample, the measured current would differ in one order of magnitude while the pressure values would remain the same.

Pressure Gauges

The positioning of the full range gauges must be well thought-out due to the strong magnetic field that surrounds them. That magnetic field may either interfere in the signal of the QMS or

influence the electric field of the heating system and thus its behavior.

The contamination of the pressure gauges cathode also occurred. This may have happened due

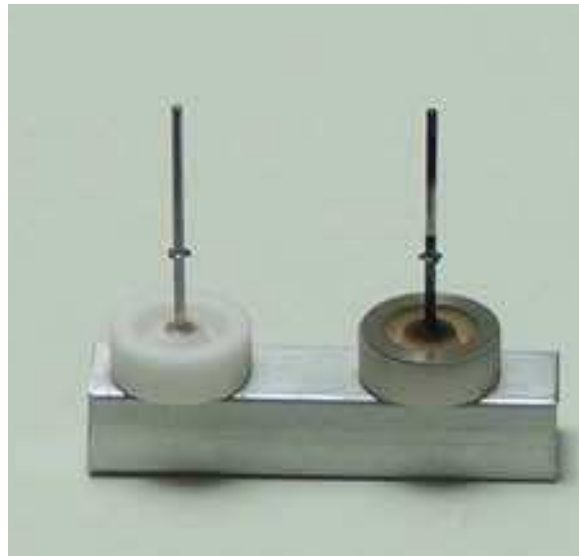


Figure 3.18: Contamination of the cathode of the full range gauge; comparison between a non (left) and a contaminated cathode (right)

to the sputtering by the ions produced in the cold discharged and lead to noise in the pressure signal. A contaminated cathode can be observed in figure 3.18.

There was also a circumstance where the controlling circuit would not activate the Penning mode. This situation resulted in a constant signal in the range of 10^{-3} mbar and to enable its future detection an additional gauge, FR3, started to be used to register the pressure.

Temperature Sensors

The main problem identified in the temperature sensors was their malfunctioning at high temperatures. This would difficult the prevention and the replacement in the beginning of the experiment. Since there were no visible signs of deterioration, this mistake was attributed to the degradation of the ceramic insulator which would then allow the contact between the two detection copper wires. The fact this event was observed several times weighted on the decision in reducing the number of sensors used in the apparatus.

3.3 Specimens

3.3.1 Sample Description

The samples measured in this work were sections of an austenitic stainless steel tube. Two samples of each producer were measured (A1 and A2 for producer A shown in figure 4.2), one of them at least twice (signalled with T1 and T2 in figure 4.2).

3.3.2 Probe Assembly

In both ends of the samples covers and a tube were weld.



Figure 3.19: Assembled probe; section of a ASS tube where two steel covers (one flat and other with a hole where is welded a 12 mm diameter steel tube) are welded in both ends. The specimen is introduced in a CF blank flange, fixed recurring to a *Swagelok* squeeze connection and a sensor is wired at the middle of its length

The probe was then polished on the outer surface with a P120 grit abrasive paper to remove any superficial films. It was then placed at the centre of a 150 mm diameter CF blank flange with a feedthrough to allow the connection between the sensor and the data recorder unit. The probe, distanced 100 mm from the flange, was fixed recurring to a *Swagelok* squeeze connection. This distance allowed to centre the sample in the first HS. In the new one, the sample is no longer centred but this distance was kept. A sensor is then positioned in the middle of the probe and attached to its surface with a free zinc wire. The probe straightness is verified with a water mark and a leak test is performed.

The probe is finally introduced in the chamber, the isolation between apparatus and power supply is verified with a multimeter and the chamber is closed screwing the recipient and probe flanges with a torque wrench at 15N/m force.

3.4 Experimental Procedure

The experimental principle can be viewed in figure 3.20: hydrogen is introduced in the sample, permeates through the stainless steel tube and is lead out of the chamber by TP2. Gauges PKR2/PKR4 measure the pressure increase while gauge PKR3 is only used to check the pressure at the tubing before opening the valve.

The experimental procedure can be divided into first and second pumping stage (PS1 and PS2), baseline (SS1) and permeation stage (SS2). Figure 3.21 shows a measurement profile where each of the stages are signalized. The first increase of pressure verifies when the HS is switched on (PS2). The second when TP1 is switched off, allowing the base signal to be drawn (SS1). In the figure it can also be observed that after the introduction of hydrogen (in the beginning of SS2), the increase of pressure in the chamber is not immediate and after a period of time the pressure reaches a constant value (SS2).

3.4.1 Procedure Description

The description below will take chamber 1, left side of figure 3.2, as an example.

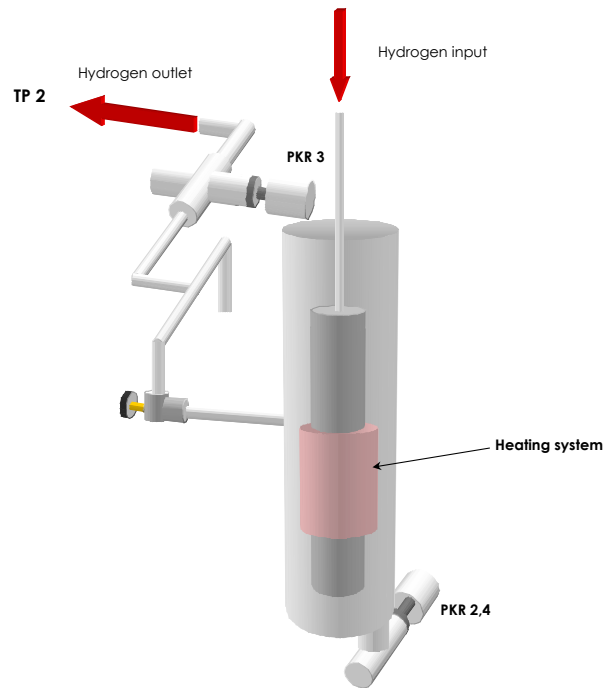


Figure 3.20: Detailed view of a measuring chamber, full range gauge positioning, intermediary piping and flow direction

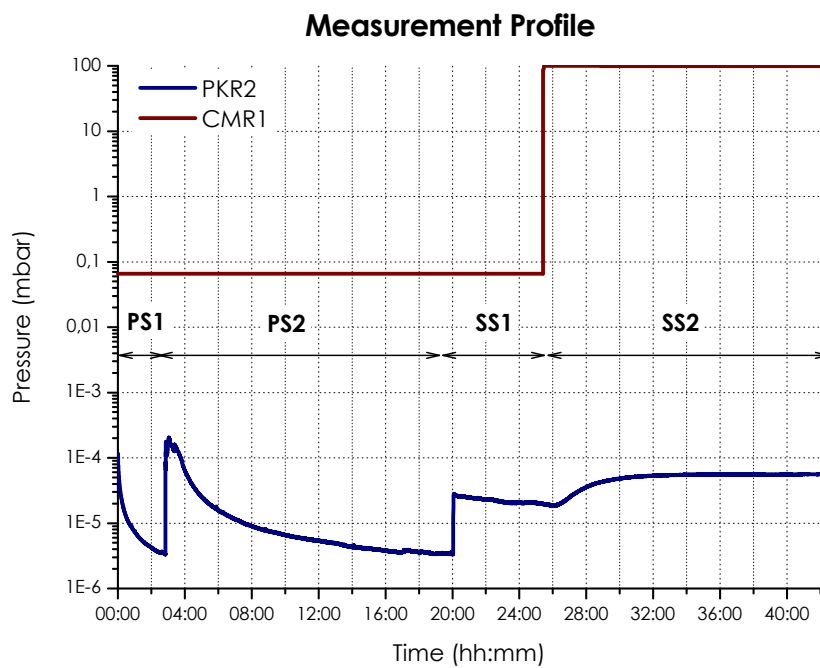


Figure 3.21: Measurement profile and stage identification. Time presented in hours and pressure in mbar

Initial Pumping Stage

This stage has the aim of preventing an aggressive oxidation in the chamber and sample.

1. Assure that RVP1, RVP2, RVP3 and TP2 are switched on;
2. after introducing the sample in the chamber slowly open valves VV1, VV2, VV4 and VV5,
3. wait until pressure is lower than 5×10^{-4} Pa, (5×10^{-6} mbar), approximately 4 hours with the present equipment.

Second Pumping Stage

This stage is designated by PS2.

1. Switch the heating system on,
2. let the pumping curve be drawn for at least 15 hours

Baseline

The baseline is the line correspondent to the base signal.

1. Close VV1,
2. open VV3,
3. let the baseline be drawn for 5 hours.

Permeation Stage

In this stage hydrogen is introduced and after a period of time, the permeation steady state is reached.

1. Switch TP1 off,
2. close VV2 and VV4,
3. open VV6 and VV7,
4. open VV10 and close it as soon as the pressure in the manometer from the bottle increases,
5. open VV9 to pump the connection to the hydrogen bottle with P3,
6. close VV9,
7. recurring to the needle valve, VV13, introduce hydrogen until the pressure reaches 100 mbar or 1×10^4 Pa (value in CMR3).
8. Close VV13 completely and open VV6 to remove the remaining hydrogen,
9. wait 17 hours

End of Experiment

1. Switch the heating system off,
2. close valves VV6 and VV7,
3. close VV3 and open VV4,
4. open slowly VV2 to pump the hydrogen from the sample and tubing,
5. close VV2, VV4 and VV5.
6. Wait until the sample has cooled down ($T < 100^{\circ}\text{C}$) to open the chamber;
7. remove the sample.

3.5 Temperature Calibration

The temperature calibration process allows (i) to acquire the temperature profile on the inner side of the sample and (ii) establish the input temperature in the controller so that the measurement temperature is achieved.

It was obtained using a temperature dummy that consisted of a sample similar to a standard one but with 16 PT 100 on its inner side distributed all over its length. Inside of the temperature dummy, a specific pressure of helium was introduced. Helium was used instead of hydrogen because it presents a similar thermal conductivity and at high pressures does not damage the PT100.

The obtained profiles are shown in figures 3.22 and 3.23. The relative position of sample, two parts of the HS, respective controlling sensors (red), top and bottom pieces of the radiation shields (grey lines) and sensors at sample surface (green) can be seen.

The profiles show that the temperature values in the central zone are higher than in the ends. This might be explained by the fact that the radiation shields in the central area help to diminish the heat dissipation through the chamber walls and feedthroughs. It may also indicate the successful role of the top and bottom radiation shields in keeping the ends cold and thus reducing the effect of the welding seams in the experimental results.

The fifteen registered temperatures (one of the sensors stopped working) are displayed along with the respective position in table 3.4. The average of these values, presented in bold, give the measurement temperature for each chamber this is approximately, $T_{\text{meas}} = 390^{\circ}\text{C}$ which corresponds to 663 K.

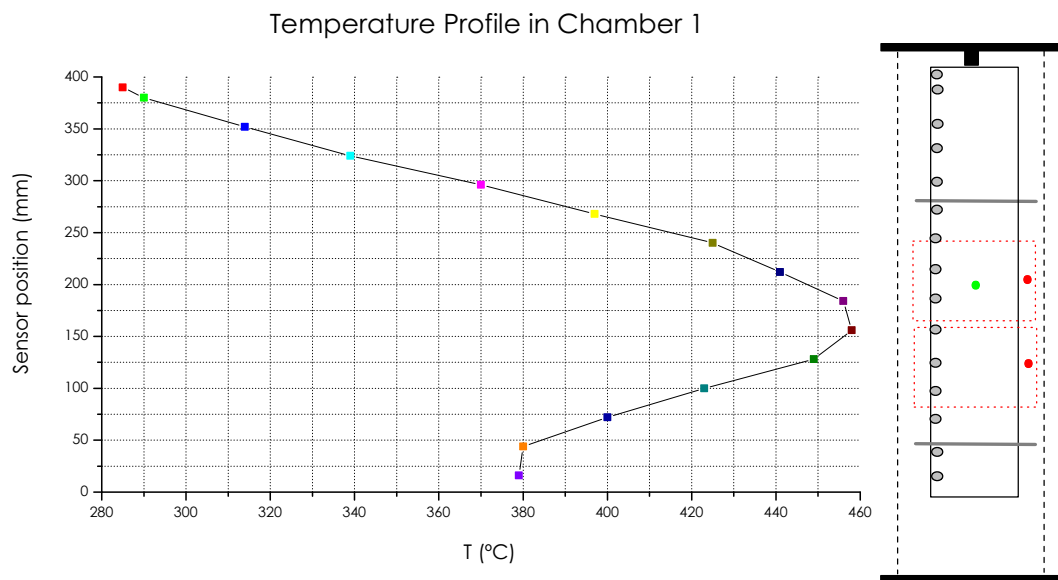


Figure 3.22: Temperature Profile of the sample in chamber 1; heating parts (red rectangles), controlling (red points) and sample sensors (green), radiation shields and sample relative positioning.

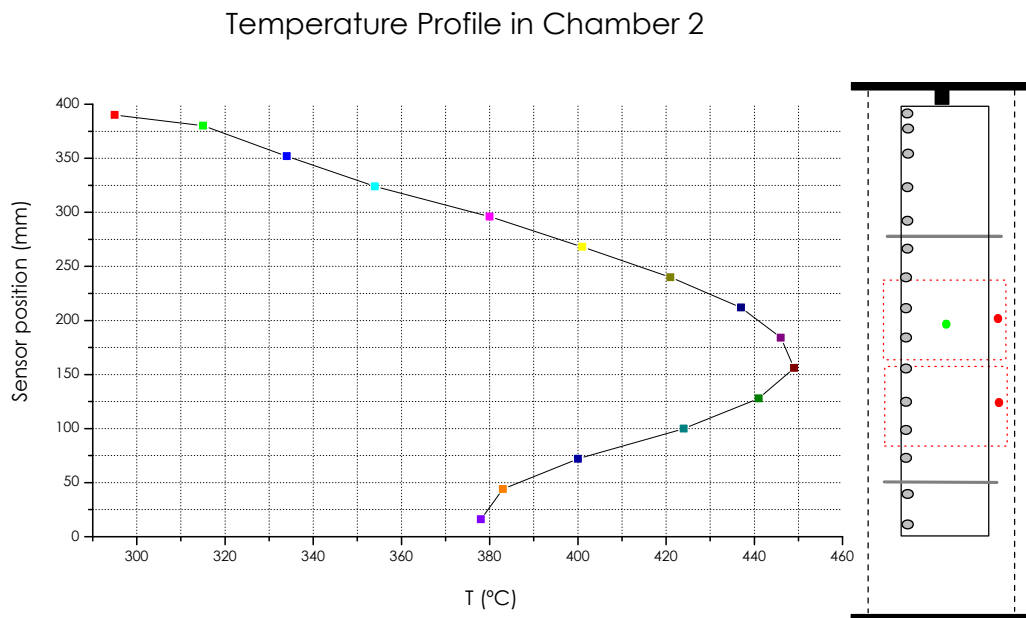


Figure 3.23: Temperature Profile of the sample in chamber 2; heating parts (red rectangles), controlling (red points) and sample sensors (green), radiation shields and sample relative positioning.

Table 3.4: Temperatures the Sample and average for each chamber; position in mm and temperatures in °C

Position	Temperature	
	Chamber 1	Chamber 2
16	295	285
44	315	290
72	334	314
100	354	339
128	380	370
156	401	397
184	421	425
212	437	441
240	446	456
268	449	458
296	441	449
324	424	423
352	400	400
380	383	380
390	378	379
Average Value	391	387

Chapter 4

Analysis of the Results

Two sets of data were analyzed: one from the PMD developed in this work and the other from a PMD located in the Max Planck Institute fuer Plasma Physik in Garching. The use of the later data set, referred to as IPP, will allow a better evaluation of the experimental conditions of this work. The analysis of the experimental data will be performed in S.I. units and will comprehend the worst case scenario.

4.1 Results from Institute fuer Plasma Physik

4.1.1 Experimental Details

The tests were performed at different temperature and pressure conditions on an unoxidized and oxidized sample that didn't suffer cold work as the specimens measured in the current work (in the bending process during the tube production).

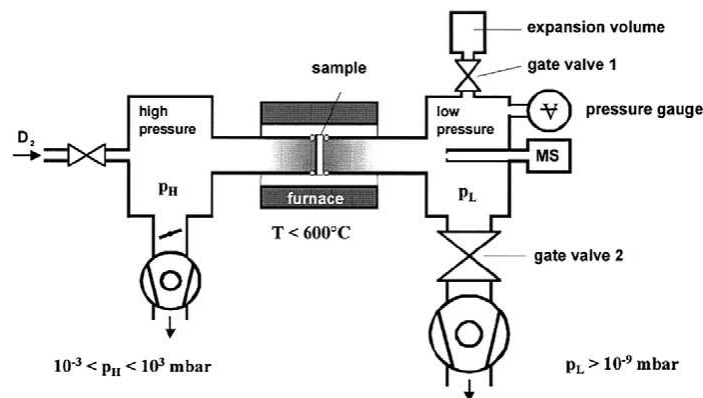


Figure 4.1: IPP Permeation Measurement Device [48]; deuterium is introduced in the high pressure volume; the low pressure volume is continuously pumped

Figure 4.1 shows the set-up of the device. The sample (with sealing provided by two gold rings), heated by the electric furnace, divides the set up in high and low pressure volumes (the last one kept at a pressure lower than 10^{-5} Pa). Deuterium is introduced in the high pressure volume. The permeated gas amount is detected with a QMS and the gas is continuously pumped of the low pressure volume (dynamic regime).

The measurement of permeation for several pressures was performed in steps: when the steady state for lower pressures is reached, the pressure in the high pressure volume is increased.

4.1.2 Data Analysis

This section describes how the values of permeability, ϕ_0 and activation energy, H_ϕ were obtained.

From equation 2.30 we have

$$\ln\phi = \ln\phi_0 + \left(\frac{-H_\phi}{RT}\right) \quad (4.1)$$

where H_ϕ is in J/mol and T in Kelvin.

Equation 4.2 is also valid:

$$\ln\phi = \ln\phi_0 + \left(\frac{-H_\phi}{R}\right) \left(\frac{1000}{T}\right) \quad (4.2)$$

but in this case the activation energy is given in kJ/ mol.

The determination of the permeability and activation energy is made through the relations 4.3 and 4.4:

$$\phi_0 = \exp(A) \quad (4.3)$$

and

$$H_\phi = -B \times R \quad (4.4)$$

4.2 Analysis of the Experimental Data

4.2.1 Area of the Sample and Pumping Speed

The calculated inner superficial area of the sample was:

$$A_{is} = 0,0827\text{m}^2$$

The pumping speed used in the determinations that follow, was the maximum pumping speed from TP1 alleged by the supplier.

In SS1 the predominant atmosphere present in the chamber is air which is constituted in its majority by N_2 . For this reason $s_1 = s_{max}(\text{N}_2) = 1 \times 10^{-2} \text{m}^3 \text{s}^{-1}$.

In SS2 the main gas present is H_2 , therefore s_2 corresponds to s_{max} for H_2 , $s_2 = 3,7 \times 10^{-3} \text{m}^3 \text{s}^{-1}$.

4.2.2 Determination of the Steady State Flux and Permeability

Through equations 2.5, 2.6 and 2.31 we are able to obtain a relation between pressure and flux values:

$$J(t) = \frac{s_2 P(t) - s_1 P_1}{A_{is} RT} \quad (4.5)$$

where P_1 and P are the pressure previously and after the hydrogen introduction.

The positive values of the flux were then plotted in a flux versus time graphic (figures 4.2 and 4.3) and for the several trials, an average curve was determined. The flux curve can be described by equation 2.24, since the alternate series follows the conditions of the Leibniz criteria, a curve of the type of equation 4.6 can be fitted.

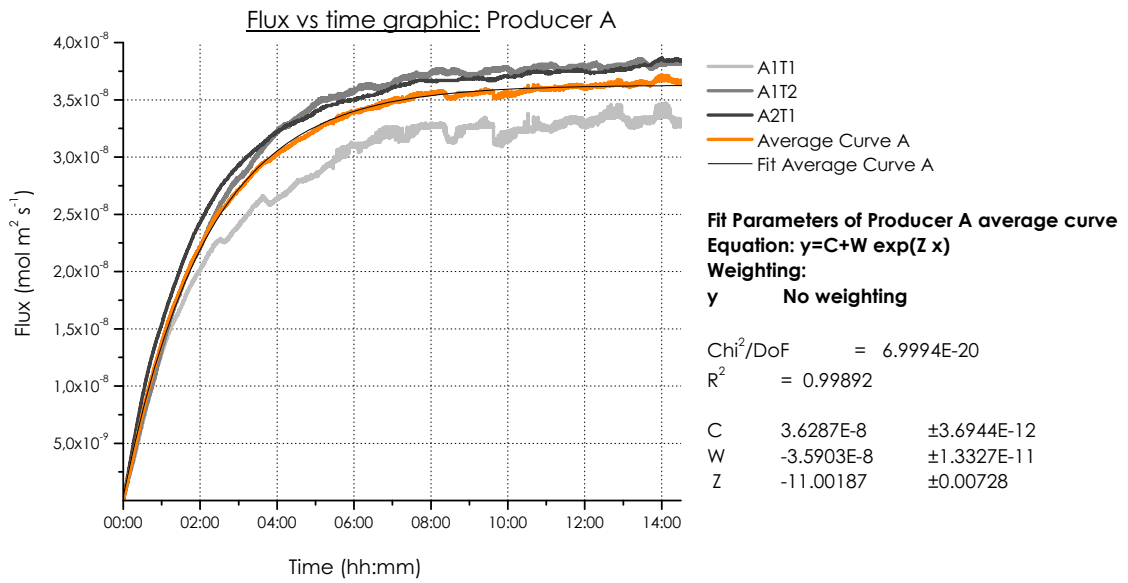


Figure 4.2: Producer A flux versus time curves, average curve fitting and respective parameters

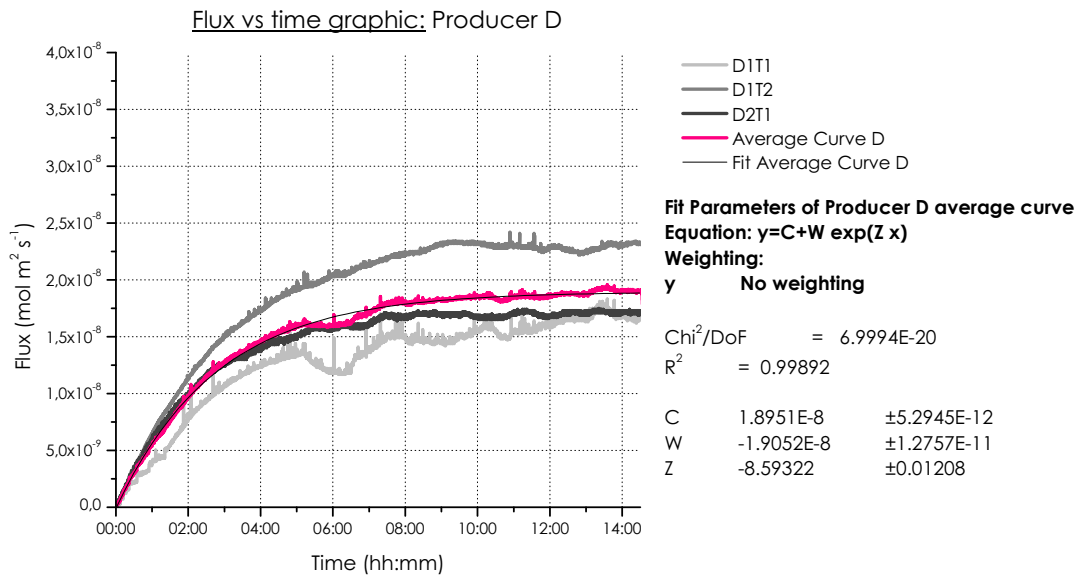


Figure 4.3: Producer D flux versus time curves, average curve fitting and respective parameters

$$y = C + W \exp(Zx) \tag{4.6}$$

The steady state flux is given by the relation 2.25 and therefore by the value of the parameter *C*.

The values of the permeability were determined through equation 2.32 and are shown, along with the correspondent flux, in table 4.1.

Table 4.1: Flux and permeability for the experimental results; data for Producer A and D, J in $\text{mol m}^{-2}\text{s}^{-1}$ and ϕ in $\text{mol m}^{-1}\text{s}^{-1}\text{Pa}^{-\frac{1}{2}}$

Producer	J	ϕ (663K)
A	$1,97 \times 10^{-10}$	$4,1 \times 10^{-16}$
D	$1,12 \times 10^{-10}$	$2,4 \times 10^{-16}$

4.2.3 Error Estimation

The permeability in function of non-derivable quantities is shown in equation 4.7.

$$\phi(t) = \frac{P(t)s l}{\pi d L P_1^{1/2}} \quad (4.7)$$

The error was evaluated through the sum of the relative errors:

$$\frac{\Delta\phi}{\phi} = \frac{\Delta P}{P} + \frac{\Delta s}{s} + \frac{\Delta l}{l} + \frac{\Delta d}{d} + \frac{\Delta L}{L} + \frac{\Delta R}{R} + \frac{\Delta T}{T} + \frac{\Delta P_1}{P_1} \quad (4.8)$$

where the variables values are listed in table 4.2.

Table 4.2: Relative Errors

Variable	Value	Description
Pressure in the measurement chamber	P 7%	estimated uncertainty
Pumping speed	s -	no information on the deviation of the maximum value thus assumed to be zero
Thickness	l 0,95%	estimated uncertainty for an instrument limit error, $l_e = 2 \times 10^{-5}$ m
Length and Diameter of the components in the apparatus	L, d 0,1%	estimated uncertainty for an instrument limit error, $L, d_e = 5 \times 10^{-5}$ m
Ideal gas constant	R 0%	$R \approx 8,314471 \text{ J mol}^{-1} \text{ K}^{-1}$, $\Delta R \approx 1,8 \times 10^{-6} \text{ J mol}^{-1} \text{ K}^{-1}$ [49]
Temperature of the measuring chamber	T 0,5%	$T \approx 663 \text{ K}$, $\Delta T < 4 \text{ K}$
Feed Pressure	P_1 2%	$P_1 \approx 1 \times 10^4 \text{ Pa}$, $\Delta P_1 < 200 \text{ Pa}$

As a result, the relative error of the permeability determined is:

$$\frac{\Delta\phi}{\phi} = 11\%$$

Chapter 5

Discussion

5.1 Reliability of data from IPP

The values of the flux were plotted as a function of the square root of the pressure. For each temperature, a fitting function of the type of equation 5.1 was drawn.

$$Y = ZX \tag{5.1}$$

The value of the slope, Z , is directly related to the value of permeability through equation 2.32.

In the obtained plot some possibilities might be considered:

- the linear relation between the flux and pressure is verified,
- the permeability increases with increasing temperature,
- the permeabilities from the unoxidized and oxidized samples tend to diverge with the temperature increase,
- the permeability of the oxidized sample is higher at 773 and 823 K.

In figure 5.1, the graphic of the permeability as a function of the temperature shows the IPP and literature (LD) curves. These consist of several ASS [19], and one particular type of SS [30], [50] and [51]. In all literature references used the surface condition was controlled during the course of the experiment.

In figure 5.1 some items can be noticed:

- IPP and LD are in the same range;
- IPP and LD values tend to converge at higher temperatures;

The last observation may indicate that the oxidation time and temperature conditions might not be the ideal to form a protective oxide layer. This can happen for two reasons (1) the atmosphere inside the oven promotes the slow growth of chromia (2) the Cr diffusion rate is not sufficiently fast.

It is worth to be mentioned however, that for the oxidized sample there was one value not to be considered in the analysis of this data. That value could either be result of a experimental error or indicate the presence of an oxide film since the obtained value of the flux is much lower than the remaining values. However experimental details are not known to allow further suppositions on this matter.

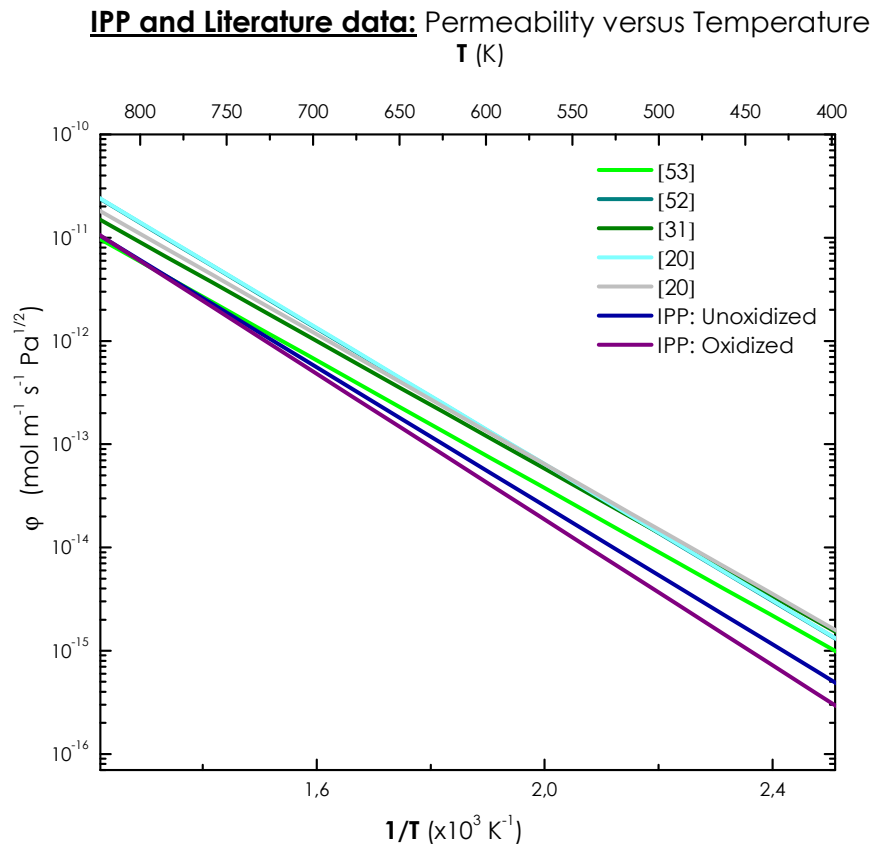


Figure 5.1: Permeability versus temperature plot for IPP and literature data; references [30] , [50] and [51] concern to one ASS type and reference [19] to the average of several ASS

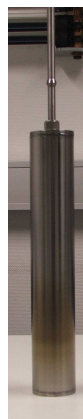


Figure 5.2: Surface condition after a measurement; yellow tonality at the samples surface might indicate the formation of an oxide film in the course of the experiment

5.2 Experimental Data

The results obtained for the permeability, as well the observation of a yellow tonality in the samples surface after its withdraw (figure 5.2), are consistent with the possible formation of a protective oxide film at the samples surface.

The differences between A and D could be explained by the fact that a smaller grain would then result in higher amount of superficial defect structures that not only favor the nucleation of the

oxide but also increase the diffusion rate of Cr. The formation of a protective oxide layer in steels with smaller grains is enhanced and the permeability reduced. Finally it must also be mentioned that the samples different provenience may have some influence in the results. However details on the tube production processes are not available impeding in this way a deeper look into this issue.

5.3 Comparison of Data

The permeabilities of the present were consistent with the ones performed in previous work [46]. The main features that differed in both works were the heating system (described in section 3.1.2) and measurement method (see section 3.1.4). Both results however differ in 2 orders of magnitude from the ones from IPP. That large discrepancy is believed to be due to the existent difference in the samples geometry resultant of the distinct production processes: more precisely the fact that the tubes suffer a cold enformation in its production process as opposed to the plain samples.

Chapter 6

Conclusions and Recommendations on Future Line of Work

The main progresses achieved in this work were:

- a more reliable heating system
- a more practical control of the heating system
- the decrease of the number of temperature sensors
- the reduction of the experimental time
- a conversion method from pressure values into permeability

The most remarkable differences between the initial and final permeation measurement devices are summarized in the table. The results obtained through pressure measurements are consistent with the ones performed with the QMS in similar measurement conditions. However the pumping speed taken into account was the maximum value provided by the producer and the presence of intermediary tubing was not considered. This last factor would lead to a lower effective pumping speed and thus to a smaller value of permeability. To determine the influence of this situation, the conductance of the device should be determined and used to calculate the effective pumping speed.

The use of the QMS was discarded because it was not possible the conversion from current values into gas amount. Unlike the pressure measurement method, the pumps maximum speed was not used in the conversion because the gauge used to record the pressure was placed too far away from the chamber. This, due to the hydrogen high conductivity, would then lead to a big temperature difference between the chamber and measuring gauge and consequently to a much lower detected pressure. For this reason, the gauge FR3 was not also taken into account in the pressure measurement results.

So far one can say this device has shown to be reliable since:

- it was able to deliver the same results for the same samples
- was able to deliver significantly different results for different samples
- and the obtained results were concordant with other works performed at similar conditions.

However an extensive testing period on diverse samples should be made, following a design of experiments plan.

This permeation measurement device reproduces quite closely the field conditions. For this reason recommendations will not be made on changing the set up. Instead, future line of work should consist in a bolder approximation to field conditions. This can be achieved by enabling the measurement of samples with the absorber coating, what will require a construction of a new temperature dummy.

Table 6.1: Differences between initial and current permeation measurement devices; only one chamber is considered in the data registry and measurement components categories

	Initial Device	Current Device
Pumping Devices	- 2 Pumping Systems constituted by a TP + RVP	
		- 1 RVP
Heating System	- metallic heating wire isolated from the skeleton with ceramic rings - rigid 3 part radiation shield with holes to position the temperature sensors	- heating wire covered with quartz - removable 3 part radiation shield with no holes
Control	- performed with FP modules through a LabView interface - 4 control sensors: 2 in each of the outer and 2 in the central heating zone	- achieved with a compact microprocessor connected to a thyristor - two control sensors positioned in each of the heating parts
Data Registry	- 8 registered temperatures (control sensors, welding seams and radiation shield) - 1 registered pressure: gauge from QMS - current value	- 1 registered temperature (middle of the sample) - 3 registered pressures: (PKR2,4; PKR3; CMR)
Measuring Method	Current	Pressure
Experimental Procedure	- 15 min PS1 and 20h PS2; - 5 h SS1 and 25h SS2; - Total= 50 h;	- 4 h PS1 and 16 h PS2; - 5 h SS1 and 15h SS2; - Total= 40 h;

According to the obtained results one can then state:

- the applied oxidation conditions seem not to be the ideal to assure the formation of a protective oxide layer in samples that present a low level of surface deformation,
- in samples with high level of surface deformation, experimental conditions may be sufficient for the build up of a protective oxide film and
- in such circumstances a smaller grain size may result in the decrease of the permeability.

The level of surface deformation, inherent to the sample geometry plays an important role in the permeability if no particular procedure is adopted to control the surface condition. However it must be recognised that these assumptions must be prudently considered since it are supported by such few permeability results.

Since specimen characteristics (size, welding seams, assembling) and experimental aspects impossibilities the use of methods to control the surface condition, further studies on this matter should consist of performing permeation measurements in oxidized samples within a larger variety of grain sizes.

Bibliography

- [1] O. Schäfer S. Teske, A. Zervos. Energy [r]evolution. Technical Report GPI REF JN 035, Greenpeace International, European Renewable Energy Council (EREC), Utrecht, The Netherlands, January 2007.
- [2] <http://www.flickr.com/photos/74424373@n00/1448540190/>, December 2008.
- [3] www.stirlingenergy.com, December 2008.
- [4] www.dlr.de, December 2008.
- [5] Dr. F. Trieb. Concentrating solar power now clean energy for sustainable development. Deutsches Zentrum für Luft und Raumfahrt e.V., 2007.
- [6] C. Richter. Concentrating solar power: status and perspectives. In *German Renewable Energy Day*. German Aerospace Center (DLR), 2008.
- [7] M. B. Muriel V. Quaschnig. Solar power: photovoltaics or solar thermal power plants. In *VGB Congress Power Plants 2001 Brussels October 10 to 12, 2001*, 2001.
- [8] N. Benz. Next generation receivers. Workshop NREL, March.
- [9] T. Wendelin A. Lewandowski H. Price, R. Forristall. Field survey of parabolic trough receiver thermal performance. Nrel/cp-550-39459, National Renewable Energy Laboratory, April 2006.
- [10] D. Blake L. Moens. Mechanism of hydrogen formation in solar parabolic trough receivers. Technical Report NREL/TP-510-42468, National Renewable Energy Laboratory, National Renewable Energy Laboratory 1617 Cole Boulevard, Golden, Colorado 80401-3393 303-275-3000, February 2008.
- [11] C. Arnold Jr. Evaluation of organic coolants for the transportation of lmfbr spent fuel rods. Report SAND77-1486, 1978.
- [12] I. Arends P. Mulder W. van Scheppingen, E. Dorrestijn. Carbon-oxygen bond strength in diphenyl ether and phenyl vinyl ether: an experimental and computational study. *J. Phys. Chem. A*, 101:5404–5411, 1997.
- [13] M. L Poutsma. Free-radical thermolysis and hydrogenolysis of model hydrocarbons relevant to processing of coal. *Energy & Fuels*, 4:113–131, 1990.
- [14] C. C. Culross S. M. Holmes L. E. Martinez B. R. Cook, B. B. Wilkinson. Hydrogen transfer induced cleavage of biaryl bonds. *Energy & Fuels*, 11:61–75, 1997.
- [15] D. Schulteiss. *Permeation Barrier For Lightweight Liquid Hydrogen Tanks*. PhD thesis, Universitat Augsburg, April 2007.

- [16] Pfeiffer Vacuum GmbH. *Arbeiten Mit Turbopumpen, Manual PT 0053 PD*, 2003.
- [17] www.ndt-ed.org, January 2009.
- [18] R.A. Oriani. The physical and metallurgical aspects of hydrogen in metals. In *ICCF4, Fourth International Conference on Cold Fusion*, 1993.
- [19] S.L. Robinson C. San Marchi, B.P. Somerday. Permeability, solubility and diffusivity of hydrogen isotopes in stainless steels at high gas pressures. *International Journal of Hydrogen Energy*, 32(1):100–116, January 2007.
- [20] J. Crank. *The Mathematics of Diffusion*. Oxford University Press, 1975.
- [21] G.J. Dienes R. J. Borg. *An Introduction to Solid State Diffusion*. Academic Press Inc., 1988.
- [22] Y. Sohn. Diffusion in solids. Lectures notes at the University of Central Florida.
- [23] H. Wipf. *Hydrogen in Metals III*. Springer, 1997.
- [24] E. Gebhardt E.Fromm. *Gase und Kohlenstoff in Metallen*. Springer, 1976.
- [25] A. Cereza. Diffusion. Department of Materials University of Oxford, 2005.
- [26] A. Chanfreau A. M. Brass. Accelerated diffusion of hydrogen along grain boundaries in nickel. *Acta Materialia*, 44:3823–3831, September 1996.
- [27] J. A. Szpunar W. T. Shmayda Y. Cao, H. Li. Effects of textures on hydrogen diffusion in nickel. *Textures of Materials, Materials Science Forum*, 91:125–129, 2002.
- [28] K.Hauffe. *Anorganische und Allgemeine Chemie in Einzeldarstellungen Band 2: reaktionen in und an festen Stoffen*. Springer, 1955.
- [29] J.Agren. Diffusion at phase boundaries. Marie Curie Summer School: Knowledge based Materials, 2004.
- [30] X. Jian S. Xiukui and L. Yiyi. Hydrogen permeation behaviour in austenitic stainless steels. *Materials Science and Engineering*, 114:179–187, July,15 1989.
- [31] H. J. Grabke R. K. Dayal. Dependence of the hydrogen permeation in stainless steel on carbon content, heat treatment and cold work. *Steel Research*, 71(6,7):255–260, 2000.
- [32] K. Sawada S. Imoto T. Tanabe, Y. Yamanishinext. Hydrogen transport in stainless steels. *Journal of Nuclear Materials*, 123(1-3):1568–1572, May 1984.
- [33] A.A. Kurdyumov Y. Belyakov;, Y. Zvezdin. Influence of the rate of oxidation of 15Cr2Mo alloy in heavy-water vapor on diffusion of the deuterium. *Journal Applied Chemistry USSR*, 47:806–808, 1974.
- [34] R.G. Derrick M.R. Louthan Jr. Hydrogen transport in austenitic stainless steels. *Corrosion Science*, 15(6-12):565–577, 1975.
- [35] A. C. Siarkowski M. R. Piggott. Hydrogen diffusion through oxide films on steel. *Journal Iron and Steel institute*, 210:901, 1972.
- [36] P.S. Flint. Usaec report kapl-659. Technical report, 1951.
- [37] P. Kofstad. *High Temperature Corrosion*. Elsevier Applied Science, 1988.

- [38] H. Grabke C.Ostwald. Initial oxidation and chromium diffusion. i. effects of surface working on 9-20% Cr steels. *Corrosion Science*, 46:1113–1127, 2004.
- [39] A. Rahmel W. F. Chu. The kinetics of the reduction of chromium oxide by hydrogen. *Metallurgical and Materials Transactions*, 10(3):401–407, September 1979.
- [40] <http://en.wikipedia.org/wiki/turbomolecularpump>, February 2008.
- [41] N. Yoshimura. *Vacuum Technology Practice For Scientific Instruments*. Springer, 2008.
- [42] www.pfeiffer-vacuum.com, October 2008.
- [43] www.oerlikon.com/leyboldvacuum/, October 2008.
- [44] <http://en.wikipedia.org/wiki/pidcontroller>, March 2008.
- [45] Pfeiffer Vacuum. *Mass Spectrometer Catalogue*, 2005.
- [46] T. Gnaedig. Bestimmung der wasserstoffpermeation in receiverabsorberrohren. Master's thesis, Fachhochschule fuer Wirtschaft und Technik Berlin, November 2007.
- [47] J. Mans. *Vacuum Physics and Technology*. Springer, 2006.
- [48] H. Maier H. Bolt D. Levchuk, F. Koch. Gas-driven deuterium permeation through Al₂O₃ coated samples. *Physica Scripta*, T108, 2004.
- [49] D. B. Newell P. J. Mohr, B. N. Taylor. Codata recommended values of the fundamental physical constants:. 2007.
- [50] V. A. Maroni E. V. Deventer. Hydrogen permeation characteristics of some austenitic and nickel base alloys. *Journal of Nuclear Materials*, 92:103111, 1980.
- [51] D. Young J. Kirkaldy. Diffusion in the condensed state. *The Institute of Metals*, 1987.